nature communications

Article

https://doi.org/10.1038/s41467-024-53531-8

Epicardial transplantation of antioxidant polyurethane scaffold based human amniotic epithelial stem cell patch for myocardial infarction treatment

Received: 6 July 2023

Accepted: 14 October 2024

Jinying Li[1,2,10], **Yuejun Yao**[3,10], **Jiayi Zhou**[1,2], **Zhuoheng Yang**[1,2], **Chen Qiu**[1,2], **Yuwen Lu**[3], **Jieqi Xie**[3], **Jia Liu**[1,2], **Tuoying Jiang**[1,2], **Yaohui Kou**[1,2], **Zhen Ge**[4], **Ping Liang**[5], **Cong Qiu**[1,2], **Liyin Shen**[3], **Yang Zhu**[1,3,6] ✉, **Changyou Gao**[3,7,8] ✉ & **Luyang Yu**[1,2,9] ✉

Myocardial infarction (MI) is a leading cause of death globally. Stem cell therapy is considered a potential strategy for MI treatment. Transplantation of classic stem cells including embryonic, induced pluripotent and cardiac stem cells exhibited certain repairing effect on MI via supplementing cardiomyocytes, however, their clinical applications were blocked by problems of cell survival, differentiation, functional activity and also biosafety and ethical concerns. Here, we introduced human amniotic epithelial stem cells (hAESCs) featured with immunomodulatory activities, immune-privilege and biosafety, for constructing a stem cell cardiac patch based on porous antioxidant polyurethane (PUR), which demonstrated decent hAESCs compatibility. In rats, the administration of PUR-hAESC patch significantly reduced fibrosis and facilitated vascularization in myocardium after MI and consequently improved cardiac remodeling and function. Mechanistically, the patch provides a beneficial microenvironment for cardiac repair by facilitating a desirable immune response, paracrine modulation and limited oxidative milieu. Our findings may provide a potential therapeutic strategy for MI.

Myocardial infarction (MI), caused by ischemia after blockage of the coronary arteries, is a leading cause of death, which affects more than 7 million individuals worldwide each year[1,2]. In the infarcted heart, extensive cardiomyocytes (CMs) death and blood vessel damage result in the release of proinflammatory mediators, including reactive oxygen species (ROS) and proinflammatory cytokines. The intense inflammatory response in the infarcted area and nearby tissues delays repair, aggravates myocardial damage, and leads to fibrosis, which is

---

[1]Zhejiang Key Laboratory of Cardiovascular Intervention and Precision Medicine of Sir Run Run Shaw Hospital, Zhejiang University-Lishui Joint Innovation Center for Life and Health, Zhejiang University, Hangzhou 310058, China. [2]College of Life Sciences-iCell Biotechnology Regenerative Biomedicine Laboratory, College of Life Sciences, Zhejiang University, Hangzhou 310058, China. [3]MOE Key Laboratory of Macromolecular Synthesis and Functionalization, Department of Polymer Science and Engineering, Zhejiang University, Hangzhou 310058, China. [4]Key Laboratory of Neuropsychiatric Drug Research of Zhejiang Province, School of Pharmaceutical Sciences, Hangzhou Medical College, Hangzhou 310013, China. [5]Institute of Translational Medicine, Zhejiang University, Hangzhou 310029, China. [6]State Key Laboratory of Transvascular Implantation Devices, Binjiang Institute of Zhejiang University, Hangzhou 310053, China. [7]Center for Healthcare Materials, Shaoxing Institute, Zhejiang University, Shaoxing 312099, China. [8]Dr. Li Dak Sum & Yip Yio Chin Center for Stem Cell and Regenerative Medicine, Zhejiang University, Hangzhou 310058, China. [9]Cancer Center, Zhejiang University, Hangzhou 310058, China. [10]These authors contributed equally: Jinying Li, Yuejun Yao. ✉e-mail: zhuyang@zju.edu.cn; cygao@zju.edu.cn; luyangyu@zju.edu.cn

associated with adverse tissue remodeling and consequent cardiac failure after MI[3,4]. However, studies have shown that extensive suppression of inflammation during cardiac repair did not improve heart wound healing[5,6]. Glucocorticoids and nonsteroidal anti-inflammatory drugs were associated with recurrent MI and higher mortality in patients with MI[7]. To date, no approved therapy can decrease the infarct size due to the irreversible death of CMs.

Stem cell-based therapies have gained attention as a promising strategy for cardiac repair after infarction in recent years[8,9]. Aiming to CM supplementation, several types of stem cells, represented by embryonic stem cells (ESCs), induced pluripotent stem cells (iPSCs) and cardiac stem cells (CSCs), have been introduced into the infarcted heart to help reduce ischemic injury in preclinical and clinical trials[10]. Although this strategy has achieved certain results, the transplanted cells demonstrated different degrees of differentiation, and low rates of integration and survival, as well as abnormal electrophysiological and mechanical functions of the repaired heart, which could increase the risk of arrhythmia[11]. All these problems combining issues of tumorigenesis, immune rejection, gene mutation and ethical concerns limit the clinical application[12,13]. Recently, experimental and clinical evidence has proved that the main role of adult stem cells during intrinsic cardiac repair is by modulating the immune system, especially maintaining a moderate acute inflammatory activation for wound-healing, rather than directly replacing the dysfunctional myocardium[14,15]. Therefore, the development of stem cell therapy regimens suitable for regulating the MI pathological microenvironment will provide more effective intervention strategies for MI treatment.

Human amniotic epithelial stem cell (hAESC), a kind of human placental stem cells derived from fetal membranes, emerged as such a promising candidate, according to its featured properties as demonstrated in others and our previous studies[16–20]. Similar to mesenchymal

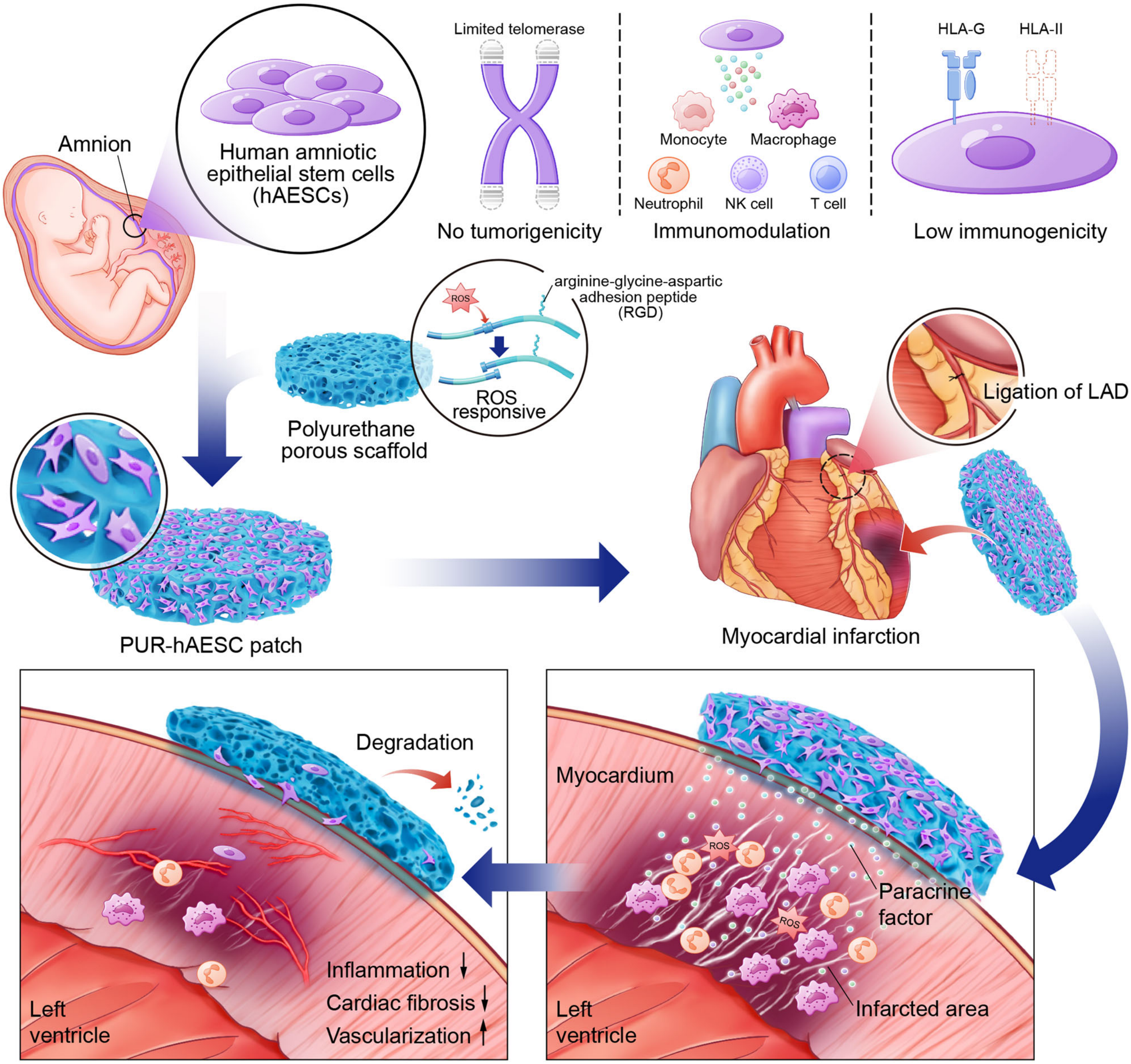

Fig. 1 | Schematic illustration of PUR-hAESC cell patch for myocardial infarction treatment. RGD modified PUR scaffold was used as a carrier for hAESCs to construct a PUR-hAESC cardiac patch. The patch provides a beneficial microenvironment for cardiac repair by facilitating a desirable immune response, paracrine modulation and limited oxidative milieu, consequently improving cardiac remodeling and function. PUR porous antioxidant polyurethane, hAESCs human amniotic epithelial cells, RGD arginine-glycine-aspartic adhesion peptide.

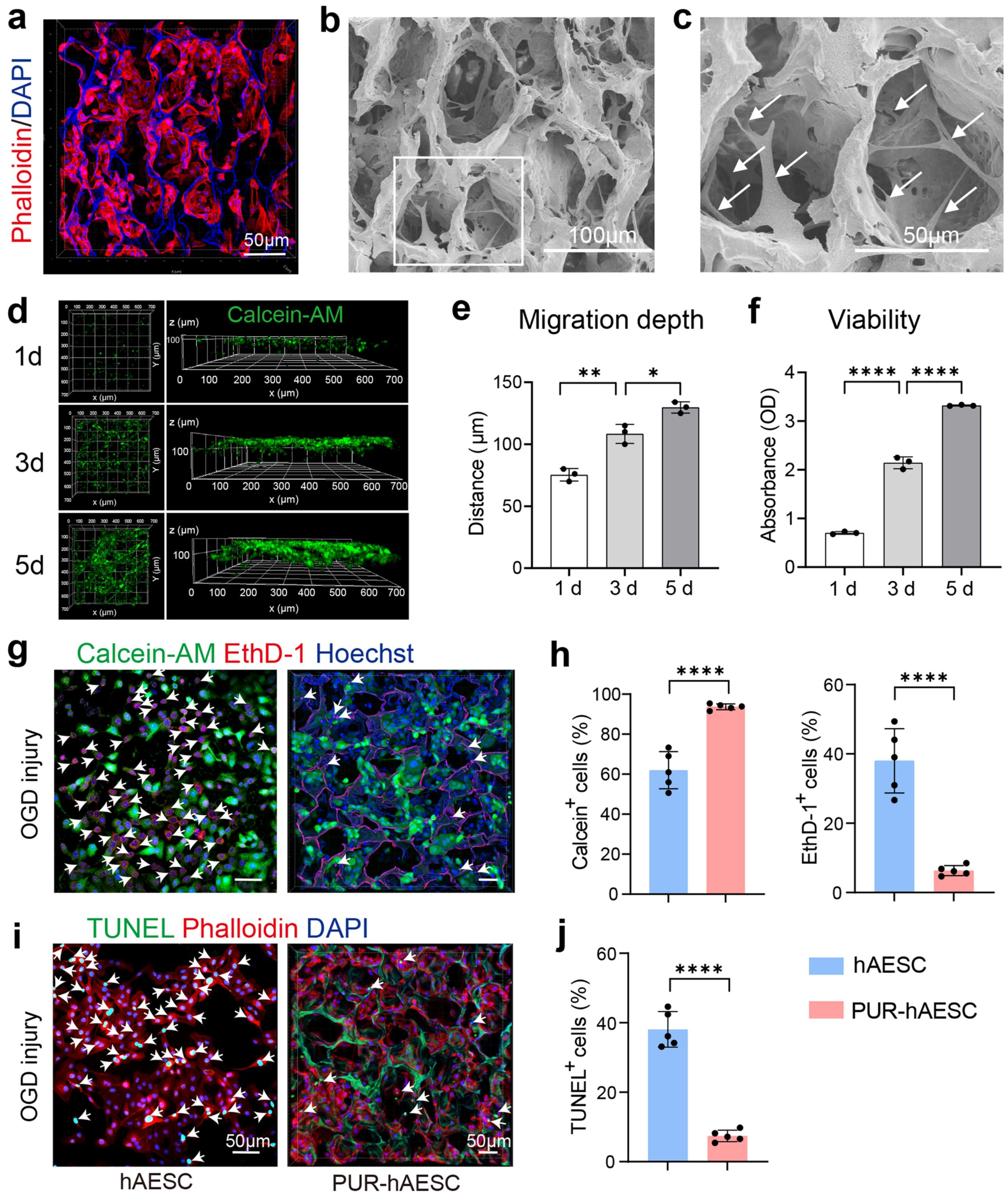

Fig. 2 | Biocompatibility of PUR scaffold with hAESCs in vitro. a Representative fluorescent image of phalloidin (red) showing the morphology of hAESCs on PUR, $n = 3$ independent experiments. **b** Representative SEM image of the PUR-hAESC patch. **c** Higher-magnification image of the white frame in **b**, white arrow indicating the migration of hAESCs cultured on PUR. **d** 3D-reconstructed confocal images of hAESCs after culture for 1, 3 and 5 days on PUR porous scaffolds. **e** Migration depth of hAESCs into the porous scaffold, 1 d vs 3 d ($p = 0.0011$), 3 d vs 5 d ($p = 0.0104$), $n = 3$ independent experiments. **f** Viability of hAESCs in PUR porous scaffold for 1, 3 and 5 days assayed via CCK-8 assay, 1 d vs 3 d ($p < 0.0001$), 3 d vs 5 d ($p < 0.0001$), $n = 3$ independent experiments. **g** Calcein-AM (live)/EthD-1 (dead) staining to determine the viability of hAESC with or without PUR scaffold after oxygen glucose deprivation (OGD) injury; quantification summary in **h**, $p < 0.0001$, $n = 5$ independent experiments. **i** TUNEL staining (green) and phalloidin staining (red) revealed the viability and morphology of hAESC on PUR scaffold after OGD injury and quantification summary in **j**, $p < 0.0001$, $n = 5$ independent experiments. Scale bar, 50 μm in **a**, **c**, **g**, **i** and 100 μm in **b**. All data are presented as means ± SD, $^*p < 0.05$, $^{**}p < 0.01$ and $^{****}p < 0.0001$ vs control, one-way ANOVA in **e** and **f**, followed by Tukey's multiple comparisons test and two-tailed unpaired *t* test in **h** and **j**.

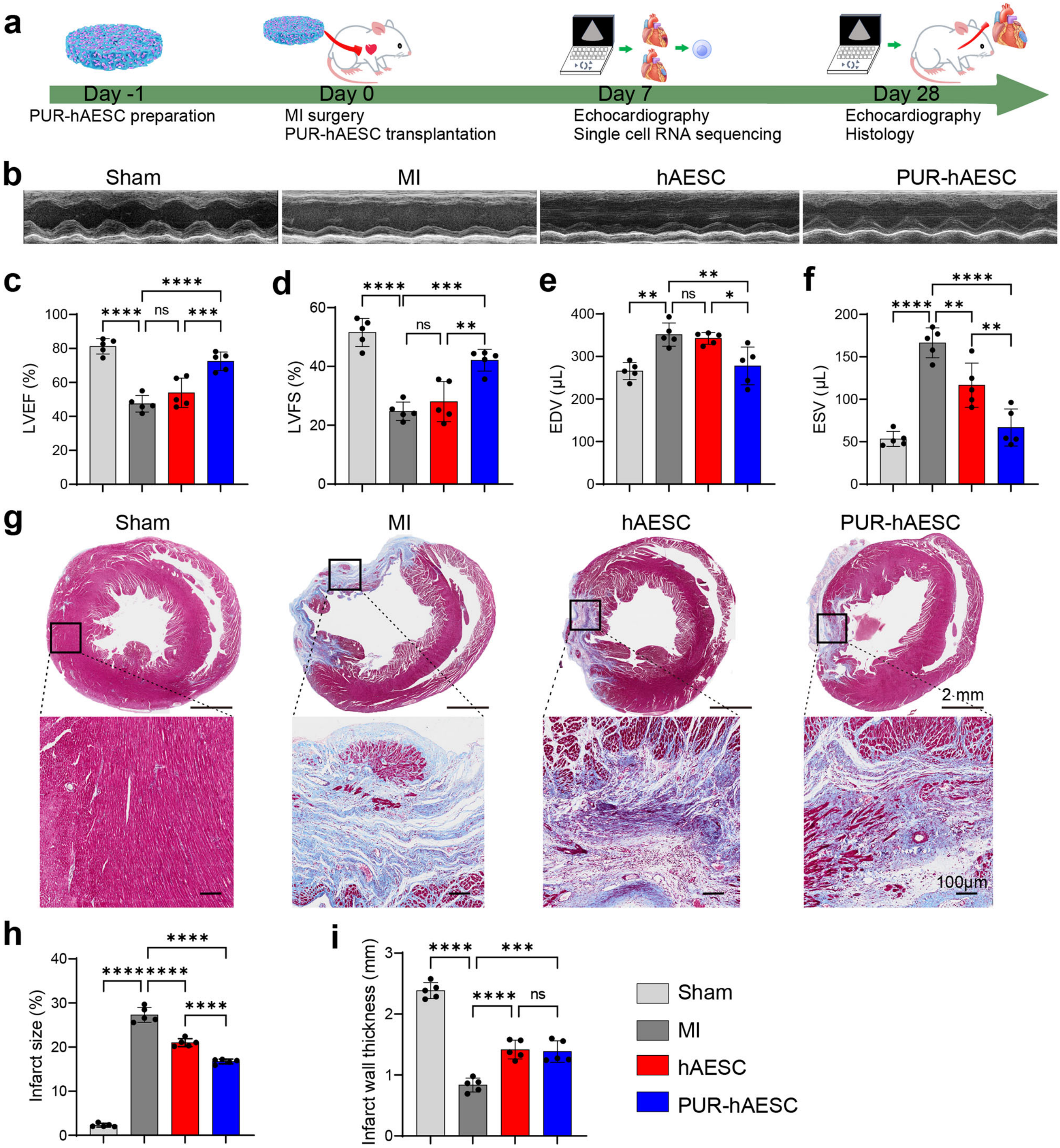

Fig. 3 | PUR-hAESC patch ameliorated ventricular dysfunction and reduced pathological cardiac remodeling after acute MI. a Schematic showing the study design. Cardiac function was assessed 7 and 28 days after MI. **b** Representative echocardiography images and quantitative analysis of **c** left ventricular ejection fraction (LVEF), **d** left ventricular fractional shortening (LVFS), **e** end-diastolic volume (EDV) and **f** end-systolic volume (ESV) by echocardiography post implantation for 28 days, sham vs MI ($p < 0.0001$ in **c**, **d**, **f**, $p = 0.0013$ in **e**), MI vs hAESC ($p = 0.3688$ in **c**, $p = 0.7070$ in **d**, $p = 0.9639$ in **e**, $p = 0.0048$ in **f**), MI vs PUR-hAESC ($p < 0.0001$ in **c** and **f**, $p = 0.0002$ in **d**, $p = 0.0047$ in **e**), hAESC vs PUR-hAESC ($p = 0.0010$ in **c**, $p = 0.0014$ in **d**, $p = 0.0123$ in **e**, $p = 0.0049$ in **f**), $n = 5$ rats per group. **g** Masson's trichrome staining of the whole heart; scale bars: 2 mm. Representative images in the infarct zones; scale bars: 100 μm. Quantitative analysis of infarction size (**h**) in the whole heart and LV wall thickness (**i**) in MI region. Normal hearts of the sham group were stained for comparison, sham vs MI ($p < 0.0001$ in **h** and **i**), MI vs hAESC ($p < 0.0001$ in **h** and **i**), MI vs PUR-hAESC ($p < 0.0001$ in **h**, $p = 0.0001$ in **i**), hAESC vs PUR-hAESC ($p < 0.0001$ in **h**, $p = 0.9856$ in **i**), n = 5 rats per group. All data are presented as means ± SD, $^{*}p < 0.05$, $^{**}p < 0.01$, $^{***}p < 0.001$ and $^{****}p < 0.0001$ vs control, ns not significant, one-way ANOVA was used for statistical analyses, followed by Tukey's multiple comparisons test.

stem cells (MSCs), hAESCs have advantages of potent paracrine effects and immune regulation[21]. Many placental cell types, including hAESCs, demonstrate immune-privilege based on the absence of human leukocyte antigen (HLA) class II molecules and the high expression of nonclassical HLA class I molecules[22]. As placenta-derived cells, hAESCs have many additional advantages, such as an abundant supply, no ethical issues, and no additional invasive procedures. As neonatal cells, hAESCs have no age- or environment-associated DNA damage compared with human adult stem cells[23]. Most importantly, the hAESC is a safe stem cell that is genetically stable and does not form tumors upon transplantation into both volunteers and patients[24,25]. Non-tumorigenicity and a lack of ethical concerns are also two major advantages of hAESCs compared with iPSCs and ESCs. More importantly, many studies have demonstrated that hAESCs exert multiple immunomodulation activities[26]. hAESCs could secrete beneficial paracrine factors with anti-fibrotic, pro-angiogenesis and immunomodulatory properties such as matrix metalloproteinases (MMP-2, MMP-9), vascular endothelial growth factor (VEGF), angiogenin (AGN), macrophage migration inhibitor factor (MIF) and indoleamine 2,3-dioxygenase (IDO), that modify surrounding cells and the microenvironment[27]. Particularly, we conducted a systematic safety evaluation of hAESCs and developed a current Good Manufacturing Practice (cGMP)-grade hAESC cellular therapy product in a serum-free system, based on our previous study[28]. Taken together, these properties make hAESCs attractive for cellular therapy of MI.

The major hurdle hampering the efficacy of cell delivery in cell therapy is the extremely low cell retention and survival rate under local pathological microenvironment[29]. Recently, biomaterials have been applied in MI therapeutics, promising to address these limitations of cell transplantation. We have been studying ROS responsive polyurethane cardiac patches over several years, demonstrating that the patch is flexible, elastic, and compatible with cell viability[30,31]. Moreover, the ROS-responsive polymers can "intelligently" consume excessive ROS and have been considered to an ideal carrier for transplanted cells[32,33]. Here, we developed a porous antioxidant polyurethane (PUR) scaffold as a carrier for hAESCs to construct a PUR-hAESC cardiac patch as illustrated in Fig. 1. To improve cell retention, the previous antioxidant polyurethane (PFTU) was modified by the arginine-glycine-aspartic adhesion peptide (RGD), which is found in fibronectin and plays a role in cellular attachment and spreading[34,35]. In this strategy, the PUR-hAESC patch offers unique advantage for hAESCs survival and significantly improved MI by mediating the microenvironment of MI.

Results

Characterization of hAESCs and PUR porous scaffold

The cultured cGMP-grade hAESCs displayed the typical epithelial appearance and marker (Supplementary Fig. 1a, b). The hAESCs were negative for the epithelial-mesenchymal transition marker N-cadherin (CD325) and the mesenchymal marker CD146 (Supplementary Fig. 1c, d), which confirmed the purity of hAESCs. The immune privilege of hAESCs was indicated by the low expression of HLA-DQ and HLA-DR (Supplementary Fig. 1e, f) and high expression of HLA-G and CD59 (Supplementary Fig. 1g, h). Moreover, hAESCs demonstrated a high secretion of beneficial cellular factors for oxidation resistance, immune modulation, ECM remodeling and angiogenesis, comparable to human umbilical cord mesenchymal stem cells (hUMSCs) (Supplementary Fig. 1i–l). Together, these results indicate that the hAESCs are a safe stem cell as a promising candidate for cell-based therapy based on their strong beneficial paracrine factors.

Based on the ROS-responsive polyurethane porous scaffold PFTU in our previous study[31], the NMR spectra of PUR scaffold showed that RGD peptides were successfully grafted onto the polyurethane backbone (Supplementary Fig. 2a). The polyurethane porous scaffolds obtained by freeze-drying have irregular porous structure with a pore size of 111.5 ± 22.4 μm and a porosity of 89.4 ± 2.2%, which provided good connectivity for the growth and migration of hAESCs (Supplementary Fig. 2b). In addition, the PUR porous scaffold had the advantage of antioxidant properties through a combination of thioketals bonds and unsaturated double bonds. More than 90% DPPH free radicals were eliminated within 1 h (Supplementary Fig. 2c). The PUR scaffold could also scavenge 21.2 ± 3.4% and 91.4 ± 2.2% superoxide anion and hydroxyl radicals in 4 h, respectively (Supplementary Fig. 2d, e). PUR degraded slowly in PBS with no visible loss of mass over a period of 4 weeks, while in hydrogen peroxide, the mass decreased noticeably from the second week, and only 40% of the mass remained in the fourth week. Moreover, the porous PUR showed small holes in the SEM image after 4 weeks of degradation (Supplementary Fig. 2f, g). These data indicated the PUR porous scaffold is a porous, antioxidant polyurethane patch scaffold as carrier for hAESCs.

Biocompatibility of PUR-hAESC patches in vitro

To optimize cell seeding efficiency, hAESCs were seeded to the PUR scaffolds with different seeding densities. The live-dead cell staining using a Calcein-AM/PI double staining kit determined 4×10^6 cells/mL is the optimal seeding density (Supplementary Fig. 3a, b). Moreover, no substantial leakage of hAESCs loaded into PUR scaffold was found, as evidenced by 80.1% loading efficacy of hAESCs after 24 h (Supplementary Fig. 3c, d). Therefore, for formal experiment, 50 μL of hAESCs at 4×10^6 cells/mL (a total of 2×10^5 cells) was seeded to each PUR scaffold.

To confirm whether the PUR scaffold had the appropriate structure and mechanical characteristics for hAESC culture, the cell morphology, proliferation and migration of hAESCs on the PUR porous scaffold were investigated. Phalloidin staining and SEM observations revealed the morphology and spreading state of hAESCs on the PUR porous scaffold over 24 h (Fig. 2a–c). hAESCs spread randomly on the surface of the PUR scaffold, and the porous structure was extensively covered by cells. It was observed that the cells protruded many pseudopods and the tentacles formed a strong interaction with the porous scaffold. Next, the migration and distribution of hAESCs in the PUR scaffold was assessed using CLSM at days 1, 3, and 5 (Fig. 2d). With continued cell culture, the density of cells increased significantly and the migration depth of cells into PUR cavity also increased (Fig. 2e). The cell viability of hAESCs cultured on PUR scaffold further indicated obvious cell proliferation (Fig. 2f). These results suggested that PUR has favorable cell compatibility, which is conducive to hAESC adhesion, spreading, and migration. Moreover, the PUR scaffold can protect hAESCs from ischemic shock by employing oxygen glucose deprivation (OGD). Live/dead and TUNEL staining revealed that the PUR scaffold retained decent viability of hAESCs (Fig. 2g, h) and significantly reduced TUNEL$^+$ cells under OGD treatment for 5 h (Fig. 2i, j). Collectively, these data suggested that the PUR scaffold was suitable for the growth of hAESCs and could promote hAESC survival under OGD injury.

The therapeutic effect of PUR-hAESC patch on MI in rats

To investigate the therapeutic potency of the PUR-hAESC patch on MI, PUR-hAESC patches were adhered to the infarcted region, while an equal number of hAESCs were delivered to the infarcted region in hAESC group. All animals were euthanized 28 days post-surgery, and hearts were harvested for histological analysis (Fig. 3a). M-mode echocardiographic images showed the LV wall motion after different treatments (Fig. 3b). In the MI group at 7 days and 28 days post-surgery, the left ventricular ejection fraction (LVEF) and left ventricular fractional shortening (LVFS) had significantly decreased compared with those in the Sham group, whereas the end-diastolic volume (EDV) and end-systolic volume (ESV) had increased, indicating the decline in cardiac function and dilation of the LV (Fig. 3c–f and Supplementary Fig. 4a–d). Compared with the MI group, directly injected hAESCs significantly improved LV dilation, although heart function was not increased. After 28 days of treatment, the hearts that received the PUR-hAESC patch transplantation had the largest LVEF and LVFS, and the smallest ESV and EDV, indicating that the contractility of the ventricle had increased and the dilation of LV had decreased, which effectively inhibited the negative remodeling of the LV (Fig. 3c–f).

H&E staining and Masson's trichrome staining revealed heart morphology and fibrosis 28 days after various treatments (Fig. 3g and

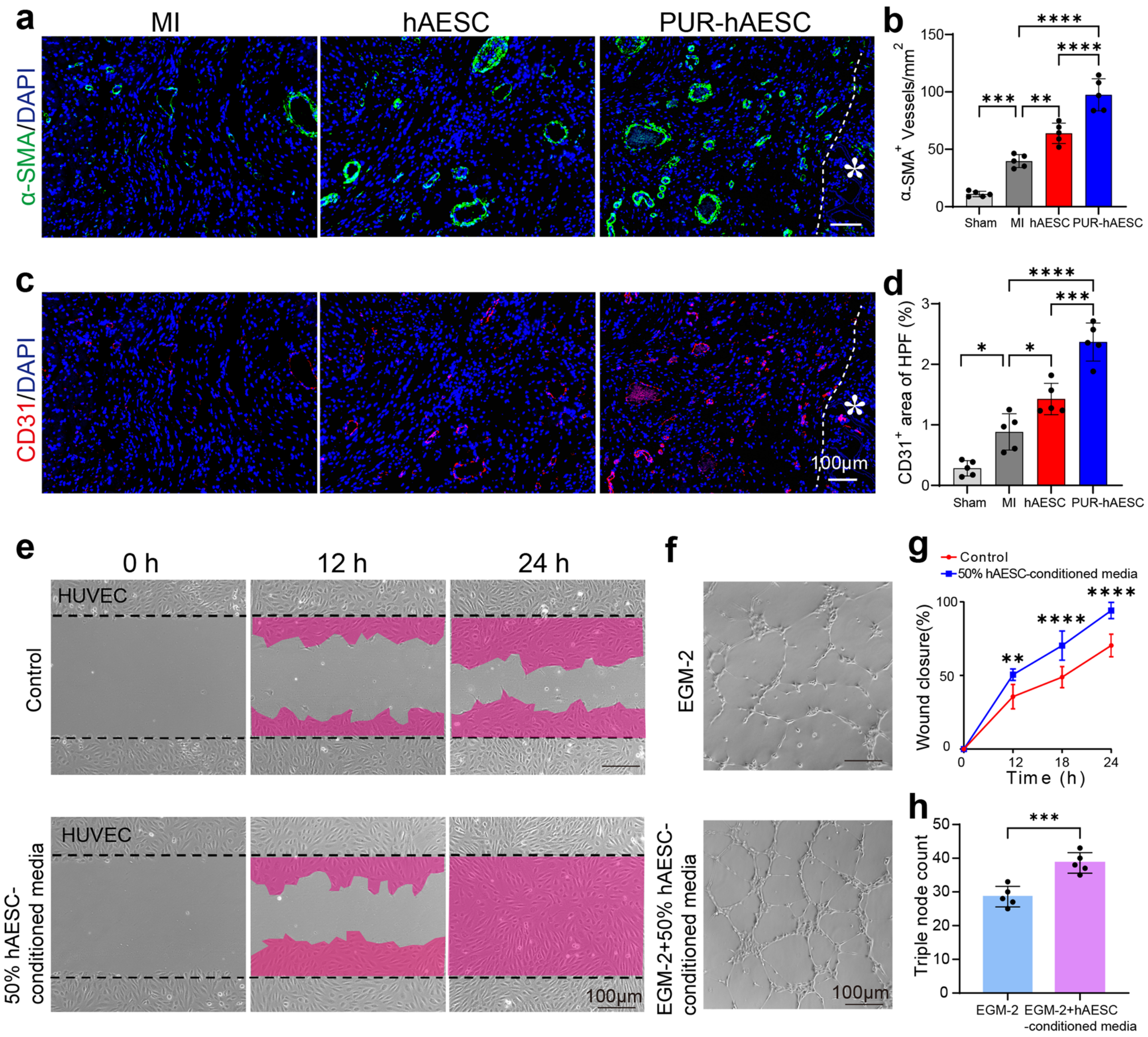

Fig. 4 | PUR-hAESC patch promoted angiomyogenesis in the post-MI heart. Representative immunofluorescent images and quantification of α-SMA$^+$ blood vessels (**a**, **b**) and CD31$^+$ area (**c**, **d**) in the infarction region post implantation for 28 days, White dashed lines indicate the border locations of the patches, and white asterisks point out the porous patch locations, Sham vs MI ($p = 0.0005$ in **b**, $p = 0.0107$ in **d**), MI vs hAESC ($p = 0.0026$ in **b**, $p = 0.0214$ in **d**), MI vs PUR-hAESC ($p < 0.0001$ in **b**, **d**), hAESC vs PUR-hAESC ($p < 0.0001$ in **b**, $p = 0.0002$ in **d**), n = 5 rats per group. **e** Phase-contrast microscope images of HUVECs to evaluate the migration capability; quantitative results are shown in **g**, 12 h ($P = 0.0033$), 18 h ($p < 0.0001$), 24 h ($p < 0.0001$), n = 5 independent experiments. **f** Representative images of tubes formed on Matrigel; quantification summary in **h**, $P = 0.0008$, n = 5 independent experiments. Scale bars: 100 μm in **a**, **c**, **e** and **f**. All data are presented as means ± SD, $^*p < 0.05$, $^{**}p < 0.01$, $^{***}p < 0.001$ and $^{****}p < 0.0001$ vs control, one-way ANOVA in **b**, **d**, followed by Tukey's multiple comparisons test; two-way ANOVA in **g**, followed by Bonferroni's multiple comparisons test and two-tailed unpaired *t* test in **h**.

Supplementary Fig. 5a, b). The LV wall of the MI group was almost completely replaced by blue-stained collagen fibers, and the ventricular cavity had become larger while the ventricular wall had thinned. In the infarct area, rats in the hAESCs and PUR-hAESC groups had retained more myocardial tissue compared with those in the MI control group. The infarcted sizes were effectively controlled by the different treatments, especially the PUR-hAESC group (Fig. 3h). Moreover, compared to MI group, hAESCs injection and PUR-hAESC transplantation had increased infarct wall thickness (Fig. 3i). These results indicated that hAESCs generated beneficial effects on ventricular wall thinning and ventricular cavity expansion after MI. The effects were more significant when combined with the PUR scaffold. We then performed gene expression analyses with rat heart tissues harvested 7 days and 28 days post-MI. Consistently, the expression of several fibrosis-related genes including collagen type I (COL1), collagen type III (COL3), were significantly downregulated in the hAESCs and PUR-hAESC groups while that of matrix metalloproteinase 9 (MMP9) was upregulated (Supplementary Fig. 6a).

In addition, the therapeutic effect of PUR-hAESC patch on MI was compared with the thermoplastic polyurethanes (TPU)-human umbilical cord mesenchymal stem cells (hUMSCs) TPU-hUMSC and PUR-hUMSC patches. For a comprehensive comparison of the therapeutic effects, TPU-hUMSC, PUR-hUMSC and PUR-hAESC patches were administrated onto the infarcted region of MI rats. As a cardiac function indicator, the echocardiography results demonstrated that PUR-hAESC transplantation had the greatest LVEF and LVFS at 7 days and 28 days after MI (Supplementary Fig. 7a, b). Moreover, Masson's trichrome staining revealed that compared to the MI group,

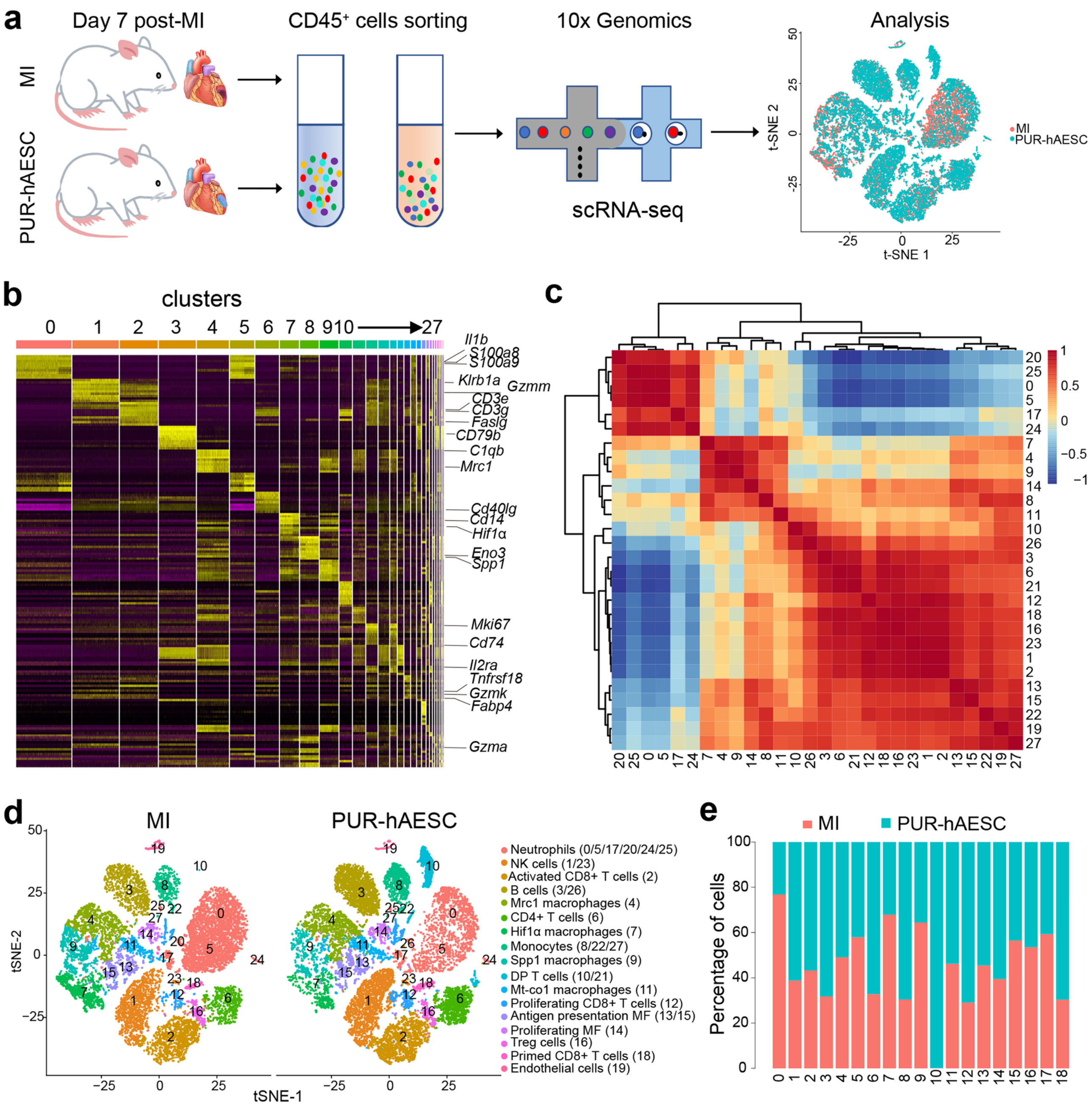

Fig. 5 | Single-cell RNA sequencing of cardiac CD45⁺ cells reveals the presence of 27 cell clusters. a Schematic overview of the experimental setup. CD45⁺ immune cells isolated from hearts of MI and PUR-hAESC group 7 days after surgery. **b** Heat map showing the top 50 most differentially expressed genes in each cluster identified through unsupervised clustering of cardiac immune cells. Purple indicates lower expression; yellow indicates higher expression. Known cell type markers strongly and specifically associated with major cell types are shown on the right. **c** Heat map representing Pearson correlations between the 27 cell populations identified through unsupervised clustering of cardiac immune cells. Pearson's correlation coefficients are shown on the right, colored according to the degree of correlation (from light dark blue to dark red). **d** t-SNE image showed the identified cell types are shown on the right. **e** Bar plot showing the proportions of cells in the 18 identified clusters.

PUR-hUMSC and PUR-hAESC groups had significantly lower infarcted area and thicker infarct wall, while the TPU-hUMSC group cannot significantly decrease cardiac fibrosis (Supplementary Fig. 7c–e). Furthermore, after 28 days of treatment, α-SMA and CD31 staining results showed a similar trend of the fibrosis results, and PUR-hAESC patch transplantation was the most effective in increasing capillary density in the infarct area, followed by PUR-hUMSC treatment (Supplementary Fig. 7f–h). Collectively, these results indicate that PUR-hAESC group is superior to TPU-hUMSC and PUR-hUMSC groups in improving cardiac function, reducing cardiac fibrosis and promoting angiogenesis, while PUR-hUMSC group has therapeutic potential to some extent but TPU-hUMSC patch does not significantly improve MI.

The pathological process of MI, especially the initial inflammatory response, is closely related to excess ROS. The imbalance between ROS production and antioxidant system can cause oxidative stress, leading to further cell apoptosis and inflammation. Excessive inflammation will, in turn, increase the production of ROS, aggravating tissue injury and cardiac remodeling, finally triggering the cardiac dysfunction and heart failure. To this end, we further compared the antioxidation functions of the three different patches in MI rats. After 1 d of infarction, the electron paramagnetic resonance

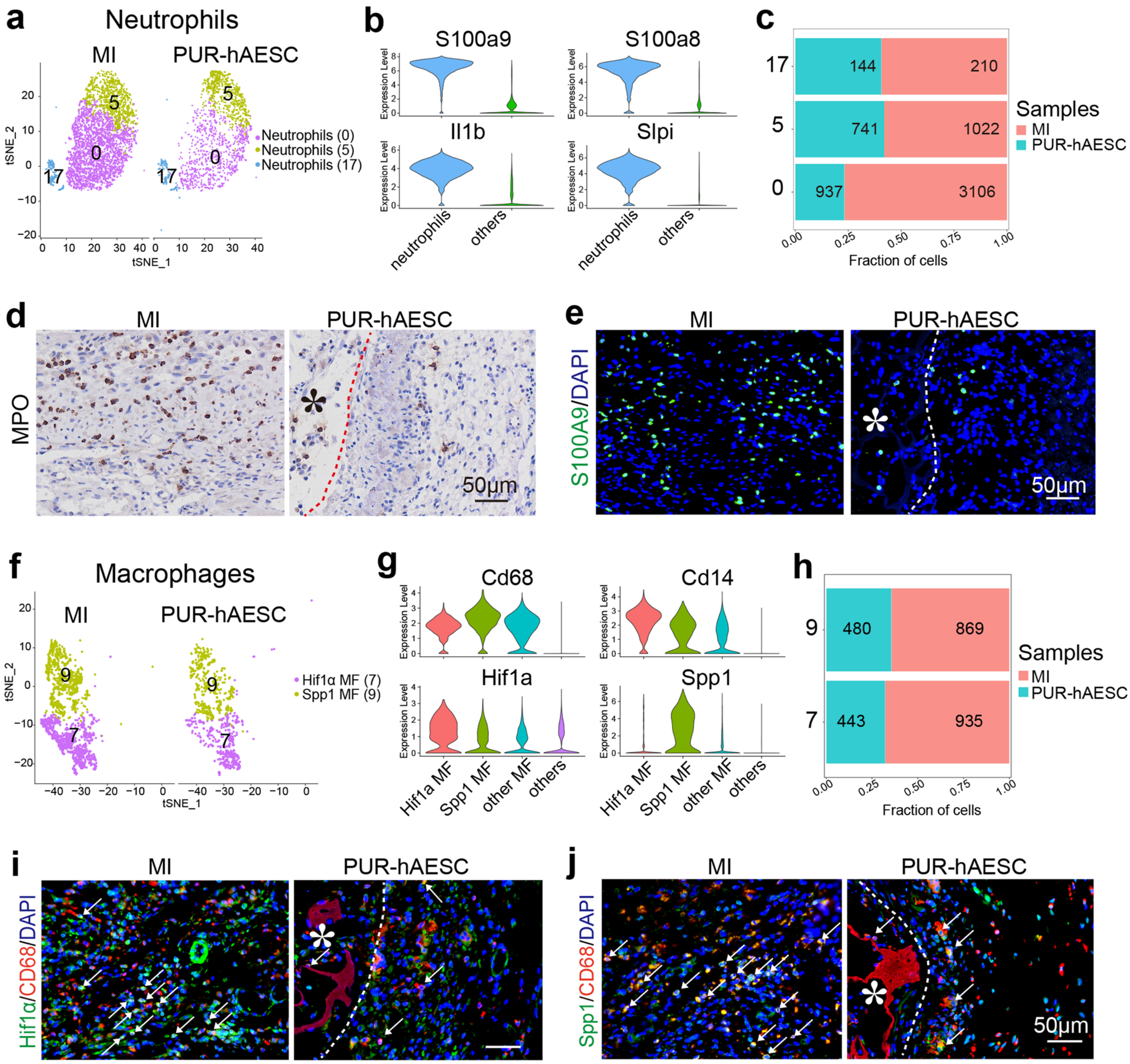

Fig. 6 | PUR-hAESC patch reduced neutrophil and inflammatory macrophage subsets. a t-SNE projection of the three neutrophil clusters identified in the heart of MI and PUR-hAESC rats. **b** Expression distribution (violin plot) showing normalized expression levels of genes encoding S100a9, S100a8, Il1b and Slpi in neutrophil clusters. **c** Bar plot showing the proportions of cells in each condition (MI and PUR-hAESC) for each neutrophil cell cluster (0, 5 and 17) identified. **d**, **e** Representative immunohistochemical and immunofluorescent images for the neutrophil cell markers MPO and S100a9 (green), n = 5 independent experiments. **f** t-SNE projection of the two macrophage clusters identified in the hearts of MI and PUR-hAESC rats. **g** Expression distribution (violin plot) showing normalized expression levels of genes encoding CD68, CD14, Hif1α and Spp1 in macrophage clusters. **h** Bar plot showing the proportions of cells in each condition (MI and PUR-hAESC) for macrophage cell cluster (7, 9) identified. **i** Representative images of immunofluorescent staining for the macrophage cell marker CD68 (red) and cluster 7 marker Hif1α (green), n = 5 independent experiments. **j** Representative images of immunofluorescent staining for the macrophage cell marker CD68 (red) and cluster 9 marker Spp1 (green), n = 5 independent experiments. Dashed lines indicate the border locations of the patches, and asterisks point out the porous patch locations. Arrows, double positive cells. Scale bars: 50 μm in **d**, **e**, **i** and **j**.

(EPR) signals representing free radicals at 3368 Gauss (G) appeared with different intensities in different group (Supplementary Fig. 8a). Quantitative results of integral area of the signal peaks and malondialdehyde (MDA) concentration revealed that PUR-hAESC group reduced the ROS level and lipid peroxidation most significantly compared to the other two patch groups (Supplementary Fig. 8b, c). The oxidative stress usually leads to the apoptosis of cells. TUNEL staining exhibited a strongest protection effect in the PUR-hAESC group, followed by the PUR-hUMSC group (Supplementary Fig. 8d, e). Therefore, among the three cell patches, the PUR-hAESC patch can better alleviate the overproduction of ROS and the subsequent oxidative damage in the infarcted myocardium.

PUR-hAESC patches promotes angiomyogenesis

To explore the underlying mechanisms of PUR-hAESC patch in improving cardiac function, we first examined the survival and proliferation of hAESCs and found that Dil-labeled hAESCs were present in both hAESCs and PUR-hAESC groups 7 days after implantation (Supplementary Fig. 9a, b). In addition, luciferase imaging demonstrated that hAESCs survived well in PUR-hAESC rats 7 days after administration, while the biological signals decreased rapidly within 3 days in hAESCs group (Supplementary Fig. 9c). To address whether the proliferation and differentiation of transplanted hAESCs toward vascular cells or cardiomyocytes had occurred, Dil and Ki67 or α-SMA or cTnT double labeling was performed. No Dil$^+$ cells expressing Ki67 or α-SMA or cTnT were found in either the hAESC or PUR-hAESC groups, indicating no proliferation and differentiation of the transplanted cells (Supplementary Fig. 9d).

Angiogenesis can restore the blood supply for the myocardium and is essential for the recovery of cardiac function after MI[36]. The immunofluorescence staining results of α-SMA and CD31 revealed that the capillaries in the hAESCs and PUR-hAESC groups were visible in the infarct area at 28 days (Fig. 4a, c). Compared with the MI group, the capillary density in the MI area was significantly increased in the hAESCs and PUR-hAESC groups after 28 days treatment (Fig. 4b, d). Furthermore, qRT-PCR analysis showed that hearts in the PUR-hAESC group had significantly upregulated expression of several angiogenesis-related genes, such as insulin-like growth factor 1 (IGF-1), fibroblast growth factor 2 (FGF2) and placental growth factor (PLGF), compared with that in the MI control hearts (Supplementary Fig. 6b). The results suggested that the PUR scaffold combined with hAESCs has the superior performance of promoting angiogenesis in the infarct area of the myocardium.

To identify detailed therapeutic mechanism of the PUR-hAESC patch, we conducted cell migration and tube formation assays using conditioned media collected from cultured hAESCs. First, we performed the scratch assay, an in vitro experiment for measuring endothelial cell (ECs) proliferation and migration, which are critical steps of angiogenesis. The addition of 50% of hAESC-conditioned media significantly enhanced the migration of human umbilical vein endothelial cells (HUVECs) and induced faster closure of the cell-free gap compared with the control group, suggesting that cytokines secreted by hAESCS enhanced the mobility of ECs (Fig. 4e, g). Next, the results from Matrigel tube-formation assay, which was performed to evaluate vessel-forming capability, showed that tube length and branches assessed 6 h later were significantly higher in the 50% hAESC-conditioned media treated HUVECs compared with untreated control HUVECs (Fig. 4f, h). Collectively, these results indicated that hAESCs directly promoted angiogenesis through the angiogenic factors secreted from hAESCs, which is consistent with our in vivo results.

PUR-hAESC patch modulates inflammatory response after MI

The moderate inflammatory response after MI is essential for the repair process, but excessive inflammation may delay the process of LV remodeling. Here, the expression levels of proinflammatory-related genes, such as interferon gamma (IFN-γ) and tumor necrosis factor alpha (TNF-α) were significantly decreased, while the expression levels of anti-inflammatory-related gene interleukin 10 (IL-10) were significantly increased in PUR-hAESC implanted hearts (Supplementary Fig. 6c). To investigate the effects of the PUR-hAESC patch on cardiac immune cells. We performed scRNA-seq analysis of sorted CD45$^+$ cells from the hearts of MI and PUR-hAESC groups 7 days after the operation using the 10× Genomics platform (Fig. 5a and Supplementary Fig. 10a, b). We identified 27 clusters, and the immune subsets in each cluster were readily identifiable based on the significant expression of well-characterized marker genes (Fig. 5b). Pearson's correlation analysis revealed groups of clusters with similar transcriptional profiles, coinciding with the main immune cell type identities (Fig. 5c). Six major immune cell populations, including macrophage, monocyte, neutrophil, T cell, B cell and natural killer (NK) cell populations, were identified based on highly variable gene expression (Fig. 5d and Supplementary Fig. 11a–k). As cluster 19 was identified as doped ECs, and the number of cells after cluster 19 was small, we limited our assessment to the first 18 clusters (Fig. 5e).

Neutrophils are the first immune cells recruited to a site of inflammation. We detected three neutrophil clusters (0, 5 and 17) and PUR-hAESC patch implantation significantly reduced the invasion of neutrophils into the infarct area compared with that in the MI heart (Fig. 6a–c). This was confirmed by immunohistochemistry and immunofluorescence staining for the neutrophil markers MPO and S100A9 in the hearts of MI and PUR-hAESC rats on day 7 after MI (Fig. 6d, e). Moreover, the macrophage population was heterogeneous, residing in and invading the infarcted myocardium. Based on previous reports[37] and their marker genes, we identified one cluster of monocyte and six types of macrophages (Supplementary Fig. 12a–k). We observed that inflammatory Hif1α and Spp1 macrophage subsets were reduced in PUR-hAESC patch group (Fig. 6f–h). These results were confirmed by immunofluorescent staining for macrophage marker CD68 and corresponding markers Hif1α and Spp1 (Fig. 6i, j).

Furthermore, we identified distinct clusters for CD8$^+$ (clusters 2, 12, and 18) T cells, CD4$^+$ (clusters 6 and 18) T cells and cluster 10 was identified as CD4$^+$CD8$^+$ double positive T (DPT) cells, which role is largely understudied. (Supplementary Fig. 13a–j). Unexpectedly, even though no DPT cells were found in hearts in the MI group, a large number DPT cells were identified in those in the PUR-hAESC treatment group (Supplementary Fig. 14a–c), which was validated by immunofluorescence staining (Supplementary Fig. 14d).

To comprehensively understand the nature of the mechanism of the PUR-hAESC therapy, the underlying connection between modulation of immune cell function and angiogenesis was further investigated for a deep analysis and validation. Consequently, we identified that the only monocyte subset (cluster 8) was reduced in the MI group and exhibited strong expression of Neuropilin-1 (Nrp1) and orphan nuclear hormone receptor (Nr4a1) (Supplementary Fig. 15a–d), which had a recognized association with angiogenesis and angiomyogenesis in cardiac repair via upregulation of vascular endothelial growth factor (VEGF)[38–41]. Immunofluorescence staining of Nrp1 and Nr4a1 in the cardiac tissues confirmed the downregulation and upregulation of the specific monocyte subset in MI and PUR-hAESC rat groups on day 7 after MI respectively (Supplementary Fig. 15e, f). Correspondingly, the immunofluorescence staining analysis also showed that the PUR-hAESC group increased the VEGF level in the infarct heart at day 28 after MI (Supplementary Fig. 15g, h). Moreover, NK cells were reported to prevent cardiac fibrosis and promote angiogenesis, involving in cardiac repair following MI[42,43]. Indeed, we found the NK cell subset (cluster 1) increased in PUR-hAESC treatment group (Supplementary Fig. 15i–k). Of note, the expression levels of activation markers CD69 and Gzmb12 were comparable in PUR-hAESC group compared to MI group, whereas that of Gzmm and Gzmk for inducing ROS production and accumulation were significantly downregulated, suggesting a responsively cardioprotective action of NK cell subset against MI based on PUR-hAESC patch (Supplementary Fig. 15l).

Factors secreted from hAESCs alleviate oxidative damage, inflammation, fibrosis and promote angiogenesis

To explore the potential beneficial effects of hAESCs on MI, we compared hAESCs and hUMSC secretome in immune regulation, angiogenesis, ECM remodeling, and antioxidant effects (Supplementary Fig. 1i–l). Furthermore, to identify the critical secreted factors from hAESCs based on the paracrine effect, we targeted on a number of highly expressed factors derived from hAESCs and designed siRNA for knockdown (Supplementary Fig. 16a–h).

Firstly, to investigate whether hAESCs-conditioned media exerted direct cytoprotective effects on cardiomyocyte. H9C2 cells were exposed to H_2O_2 for inducing ischemic injury. Administration of 50% hAESCs-conditioned media significantly improved cell viability as determined by the Annexin V assay and ROS release assay. However, when antioxidant related genes (SOD1, GSS, CAT, PRDX1) were knocked down in hAESCs, hAESCs-conditioned media cannot significantly improve cell viability (Supplementary Fig. 17a–c). The results indicated that SOD1, GSS, CAT and PRDX1 are the critical secreted factors from hAESCs for oxidation resistance.

Secondly, scRNA-seq analyses showed that the PUR-hAESC cardiac patch modulated the inflammation response through control of neutrophil and inflammatory macrophages. In vitro analysis demonstrated that treatment with 50% hAESC-conditioned media effectively down-regulated the mRNA expression of pro-inflammatory factors (IL-1β, IL-6, TNF-α) and the secretion of IL-1β, IL-6 and TNF-α in lipopolysaccharide (LPS) induced RAW264.7 macrophages (Supplementary Fig. 18a, b). The knockdown of IL1R2, CD59, PTGES and MIF all affected the immunomodulatory effect of hAESCs to varying degrees, especially when they were grouply knocked down, indicating that IL1R2, CD59, PTGES and MIF play critical roles in the immune regulation of hAESCs.

In addition, we further examined the functional effect of hAESCs on cardiac fibrosis and ECM remodeling, based on their potential properties as illustrated in Supplementary Fig. 1. Neonatal rat myocardial fibroblasts were isolated and stimulated to differentiation into myofibroblasts with treatment of TGF-β1. The myofibroblasts were then incubated with 50% hAESC-conditioned media with knocking down a number of potential critical functional genes in hAESCs including BMP1, CTSB, MMP-9. The mRNA expression of most fibrosis genes α-SMA, COL1, FN1, and CTGF were significantly decreased in treated myofibroblasts groups, except with BMP1/CTSB/MMP-9 knocking down hAESC-conditioned media (Supplementary Fig. 19a). And the expression changes of α-SMA and COL1 in myofibroblasts were further confirmed by immunostaining and western blot analysis (Supplementary Fig. 19b, c). These data revealed that hAESCs-derived MMP-9, CTSB and BMP1 are critical for ECM remodeling for MI recovery.

Moreover, based on the results shown in Fig. 4, hAESCs could directly promote angiogenesis through the secretion of angiogenic factors. To this end, further investigations were performed in cell migration and tube formation assays by treating human primary endothelial cells with 50% hAESCs-conditioned media from hAESCs with knocking down of several representative proangiogenic factors. The results indicated that VEGFA, Angiogenin1, PDGFB are the critical angiogenic factors derived from hAESCs (Supplementary Fig. 20a–d). These data may help to illustrate the major underlying mechanisms responsible for the therapeutic effects on MI, based on the paracrine effect of hAESCs in response to the post-MI microenvironment.

Discussion

In this study, we generated an antioxidant PUR-based hAESCs cardiac patch for post MI healing by providing a beneficial microenvironment for cardiac repair based on multiple facilitative factors. PUR-hAESC patch administration significantly reduced fibrosis and facilitated vascularization in the myocardium after MI and consequently improved cardiac remodeling and function. Recent studies indicated that alterations in the inflammatory environment is critical for MI repair, and the immune response after MI determines the degree of cardiac recovery[14]. Of note, the critical role of inflammation in all aspects of the myocardial injury response suggests that targeting inflammatory signaling may hold promise for reducing mortality and preventing heart failure in patients who survive acute myocardial infarction. However, the role of immune responses during post-MI repairing is still fuzzy. Studies have shown that widespread suppression of the inflammatory response during heart repair does not improve cardiac wound healing but was even associated with recurrent MI[5,7,44]. Maintaining a continuous moderate immune circumstance is a promising strategy for post-MI cardiac repairing, which, however, could not be achieved by classic immunosuppression reagents. Our previous and current data suggest a potential immunomodulatory property of hAESCs. Therefore, it is worthy to investigate the proper regulation of PUR-hAESC patch on post-MI immune environment. To this end, the effect of PUR-hAESC patch on immunomodulation was firstly focused on in the present study, which illustrates that PUR-hAESC treatment modulates both classic and non-classic functional activities immune cells by framing into a better subpopulation/phenotype. On one hand, the neutrophil and inflammatory macrophages are downregulated; PUR-hAESC patch implantation significantly limited the invasion of neutrophils and specific inflammatory macrophage subsets (Hif1α$^+$, Spp1$^+$) in the cardiac infarct area, and correspondingly expression of pro-inflammatory factors (IFN-γ, TNF-α) as well. A large number of CD4$^+$CD8$^+$ double positive T cell population (DPTs) is induced to mediate the T helper-2 (Th2) polarization of CD4$^+$ T cells for suppressing the inflammation response. Although the DPT cells have been detected in the peripheral blood and tissues in various settings in a range of human inflammatory diseases, including viral infections, autoimmune disorders and cancers[45,46], their functional role in pathological states is not fully understood and there are even few investigations about DPT in MI. Recently, observational studies suggested that DPTs could be a group of mature T cells that originates from infiltrating CD4 or CD8 single-positive T cells and develops in the periphery, rather than the result of thymocytes escaping from the thymus[47–49]. Functionally, DPTs were considered as potent immunosuppressants which favor Th2 cell polarization[50,51]. In the current study, DPTs were specifically induced in the MI area after PUR-hAESC administration with a decrease of tissue inflammation. Moreover, a CD4$^+$ T cells subset was induced correspondingly (Supplementary Fig. 13h–g). All these results indicate that promoting CD4$^+$ T cells-derived DPTs for Th2 cell polarization could be one of the critical anti-inflammation functions of PUR-hAESC patch for cardiac repair. On the other hand, specific monocyte and NK cell subsets are boosted to exert non-classic pro-angiogenic and anti-ROS functions upon PUR-hAESC treatment, correlating to other repairing beside inflammation relieving. The cellular switches mentioned above could be attributed to the ROS scavenging of the PUR scaffold and the paracrine effect of hAESCs as discussed later. These findings indicate that the PUR-hAESC patch treatment could timely facilitate the switching from inflammatory phase to reparative phase after MI for promoting the post-myocardial healing.

There have been several previous studies that describe the beneficial effects of other cell types, such as MSCs or CSCs, on MI by secreting paracrine factors[10,52,53]. Compared with cell replacement, regulating the microenvironment of injured tissue may be more effective in treating MI. To explore the potential beneficial effects of hAESCs on MI, we compared hAESCs and hUMSC secretome in immune regulation, angiogenesis, ECM remodeling, and antioxidant effects. Especially, hAESCs could secrete high levels of factors that focus on oxidation resistance while oxidative stress is concomitant with cellular injury, inflammation, and dysregulated metabolism. The results suggested that the paracrine factors derived from hAESCs might constitute the key contributors with pleiotropic effects. To further confirm the underlying mechanisms responsible for the observed effects, highly expressed factors secreted by hAESCs were selected for further validation. Intriguingly, hAESCs exert their different regulatory roles by secreting selective groups of factors; SOD1, CAT, GSS, PRDX1 for oxidation resistance, IL-1R2, CD59, MIF, PTGES for anti-inflammation, MMP9, CTSB and BMP1 for ECM remodeling and VEGF-A, Angiogenin1, PDGF-B for angiogenesis. These findings reveal that hAESCs are a promising cell source for treating MI based on their strong paracrine effect responding to pathophysiological stresses. The identification of the critical functional factors derived from hAESCs may help pre-clinical and clinical studies of PUR-hAESCs patch as potential stem-cell drug in the future.

The PUR scaffold, prepared by the PFTU with RGD polypeptides, demonstrated decent cell compatibility and suitability for the adhesion and proliferation of hAESCs. Moreover, the PUR scaffold could prevent hAESCs from the OGD injury. More importantly, the PUR-hAESC patch increased the survival rate of hAESCs in the MI zone in animal model and further improved the efficiency of cell therapy. Thereby, the PUR scaffold used in this study overcame the primary obstacle to cell-based cardiac therapy: the extremely low rate of retention and engraftment. Besides, the characteristics of PFTU itself can also directly assist in the MI injury repair due to its good elasticity for cardiac mechanical support and antioxidant capability. Our previous study proved the cardiac patch made of PFTU could scavenge excess ROS and inhibit LV remodeling and improve heart function to a certain degree[31]. The degradation rate of the ROS responsive biodegradable polyurethane material designed in this project is regulated by the ROS concentration in the tissue microenvironment, and the process of material degradation itself will consume a large amount of ROS in the microenvironment, forming a positive superposition effect. Besides, the antioxidant characteristic may also contribute to the high survival rate of hAESCs in pathological environment in vivo. Therefore, our approach may exploit the providential advantages of both PUR and hAESCs to improve the efficiency of cell therapy in MI treatment.

Aiming to reduce cardiac ischemic damage, numerous cell types have been introduced into the infarcted heart with bioengineering strategy. In the present study, we compared our PUR-hAESC patch with the TPU-hUMSC and PUR-hUMSC patches to treat MI in rat. So far, synthetic polyurethane scaffold carrying mesenchymal stem cells (MSCs) is one of the most popular bioengineering approaches for cardiac patch fabrication to treat MI, in which commercially available TPU is the general choice of scaffold due to its proper biocompatibility and flexibility. On the other side, based on the potential capability of promoting endogenous myocardial and vascular regeneration, MSCs are the most commonly used cells in cellular therapy for MI in preclinical and clinical studies. Here, we employed hUMSCs because they were reported to be the most potent hMSC source for inflammation regulation and angiomyogenesis[54]. A comprehensive comparison of the therapeutic effects unveils the best performance of the PUR-hAESC patch in post-MI cardiac repairing with superior beneficial effects on elimination of free radical, reduction of cell apoptosis, promoting myocardial repair and consequently preserving cardiac functions, compared to the other classic stem cell-based bioengineering approaches. This is mainly attributed to a comprehensive modulation with a number of superior advances of the PUR-hAESC patch. First is a specific regulation of immune responses, targeting not only the classic inflammation but also non-classic immune cell activities. Also, based on the paracrine effect of hAESCs, the secretion of pro-angiogenic factors and anti-fibrosis factors for ECM remodeling is the other major contribution to the post-MI cardiac reparative remodeling. Moreover, the decent ROS scavenging capability of the PUR-hAESC patch is another important facilitative factor for cardiac repairing.

Nonetheless, further efforts are needed to improve the therapeutic effect of the PUR-hAESC cardiac patch and promote its clinical translation. Although the ability of the PUR-hAESC patch for improving cardiac function after MI was identified, invasive open chest surgery was still required for patch implantation. Thus, mini-invasive delivery of cardiac patches should be explored for future clinical translation. Previous report indicated that small patches can be delivered and implanted into the heart surface in a minimally invasive manner[55]. PUR with elastic property can be modified with defined microfabricated lattice structure for minimally invasive delivery. Furthermore, cardiomyocytes derived from human pluripotent stem cells could be delivered with hAESCs to the MI zone through a PUR patch for both injury repair and cardiomyocytes supplementation in our future study.

In summary, our study established a comprehensive and integrative strategy combining mechanical support, “smart” ROS clearance, immune remodeling and paracrine modulation strategies for myocardial injury repair. Therefore, the PUR-hAESC cardiac patch exhibited an attractive therapeutic effect on MI. Our work may provide an antioxidant cell delivery scaffold and a more clinically relevant therapeutic system for biotherapy of cardiac diseases in the future.

Methods

Isolation and characterization of hAESCs

Fresh amniotic membranes were collected from human placentas after cesarean deliveries as described in our previous methods[20]. The procedure was approved by the Institutional Patients and Ethics Committee of the Second Affiliated Hospital of Zhejiang University School of Medicine (Ethics Code: 2020-799). All donors were negative for hepatitis A, B, C, and D as well as HIV-I and Treponema pallidum antibodies. Briefly, amnions were isolated, and blood and mucus were then carefully removed with sterile saline. Then, the amnion was incubated with 0.25%trypsin/EDTA for 20 min at 37 °C, and the sample suspension was centrifuged for 10 min at 300 g. Cells were suspended in the complete culture medium (Dulbecco’s Modified Eagle medium/F12), added with 10% KnockOut Serum Replacement (KSR), 1% non-essential amino acid, 1% antibiotic-antimycotic, 2 mM glutamine (all from Thermo Fisher Scientific, Waltham, MA, USA) and 10 ng/mL human EGF (Peprotech, Rocky Hill, NJ, United States, Cat# AF-100-15), and incubated in 5% CO_2 atmosphere at 37 °C. hAESCs were stained by mouse anti-Pan Cytokeratin (Thermo Fisher Scientific Cat# MA5-28561, RRID:AB_2745520) through immunostaining.

Flow cytometry

hAESCs were then stained with CD325 (BioLegend Cat# 350808, RRID: AB_10960145) and CD146 (BioLegend Cat# 361006, RRID: AB_2562981) for purity identification. To analyze the expression levels of HLA-DR (BioLegend, Cat# 307603, RRID: AB_314681), HLA-DQ (BioLegend, Cat#318104, RRID: AB_604128), HLA-G (BioLegend, Cat# 335909, RRID: AB_10900805) and CD59 (BioLegend Cat# 304711, RRID: AB_2819929), hAESCs were collected after incubation with 10 ng mL-1 IFN-γ (Peprotech, Cat# 300-02-100) for 72 h. The corresponding isotype controls were APC Mouse IgG1 (CD325, BioLegend Cat# 400121, RRID:AB_326443), PE Mouse IgG1 (CD146, BioLegend Cat# 400113, RRID:AB_326435), PE Mouse IgG2a (HLA-DR, BioLegend, Cat# 400207, RRID:AB_2884007), FITC Mouse IgG1 (HLA-DQ, BioLegend, Cat# 400109, RRID:AB_2861401) and APC Mouse IgG2a (HLA-G, CD59, BioLegend, Cat# 400220, RRID:AB_326468) according to the manufacturer’s instructions, and then they were analyzed by flow cytometry (FACSCalibur; BD Biosciences, Franklin Lakes, NJ). Analyses were performed using three biological replicates.

Secretory proteomic detection

After the growth of primary hAESCs and human umbilical cord mesenchymal stem cells (hUMSCs, Cat# SHTBA0009C1BAC23 obtained from iCell Biological Technology Co., Ltd., Shanghai, China) reached 80% of the substrate area, the culture medium without FBS and phenol red was replaced. After 48 h of culture, the supernatant was collected and centrifuged at 200 g at 4 °C for 5 min to remove the cells. The supernatant was collected and centrifuged at 1000 g at 4 °C for 10 min to remove cell debris. The supernatant was collected and tested by Lianchuan Biotechnology Co., LTD. Bioinformatic analysis was performed using the OmicStudio tools at https://www.omicstudio.cn/tool.

Fabrication and characterization of PUR scaffold

Polyurethane was synthesized as reported previously[31], which contains unsaturated poly (propylene fumarate) segments and ROS-responsive poly (thioketal). To improve cell adhesion, the ROS-responsive polyurethane (PFTU) was modified by the arginine-glycine-aspartic-cysteine adhesion peptide (CRGD) (Gill Biochemical, Shanghai Co., Ltd) through a click reaction. Briefly, PFTU and CRGD were dissolved in 1, 4-dioxane with a small amount of pyridine as a catalyst, and reacted at 37 °C under nitrogen protection for 24 h. The obtained RGD-grafted polyurethane (PUR) was precipitated in cold ethanol for three times, washed with ultrapure water, placed in −20 °C overnight, and finally freeze-dried for 48 h to obtain a dry PUR. The chemical structure of the PUR was performed with ^{1}H-NMR spectroscopy by dissolved in DMSO-*d6* hydrogen nuclear magnetic resonance spectroscopy (Bruker DMX500 equipment operated at 500 MHz using DMSO-d6 as solvent and tetramethylsilane as reference).

The porous scaffold was fabricated by a thermally-induced phase separation technique. First, the PUR was dissolved in 1, 4-dioxane with a concentration of 8% w/v. The solution was poured into 8-mm diameter polyethylene molds, and maintained at 4 °C for 1 h before frozen at −20 °C overnight. After freeze-dried under vacuum (<100 Pa) at −20 °C for 48 h, the PUR porous scaffold was obtained.

The morphology of the PUR porous scaffold was observed by scanning electron microscope (SEM, S-4800, Hitachi, Japan), and the pore sizes was measured and statistically analyzed by ImageJ software. The porosity of the PUR porous scaffold was measured by the absolute ethanol immersion method. For the antioxidant activity of PUR, the free radical elimination ability was detected with the 1,1-diphenyl-2-picrylhydrazyl (DHHP) assay: 10 mg PUR porous scaffold was soaked in DPPH/ethanol at 37 °C at certain time point. Percentage inhibition was evaluated by the absorbance of the solution at 517 nm, $\%\ \text{inhibition} = (AB - AS)/AB \times 100$, where AB is the absorbance of DPPH only and AS is the absorbance of DPPH with PUR. The scavenging of superoxide anion radicals was assessed using the superoxide anion assay kit (A052-1-1, Nanjing jiancheng Bioengineering Institute, Nanjing, China) and the scavenging of hydroxyl radicals was assessed using the Fenton reaction[56]. To measure the degradation of the PUR scaffold, the dry patches were weighed (W0) and incubated in PBS or 100 mM hydrogen peroxide (H_2O_2) solution at 37 °C, respectively. The samples were removed at the indicated time points and rinsed with water, dried in a freeze dryer and then weighed for residual weight of the samples (W1). Weight remaining (%) = W1/W0 × 100%.

The evaluation of cell compatibility in vitro

The PUR scaffold with a diameter of 8 mm and a thickness of 500 μm was immersed in 75% ethanol for 30 min to sterilize and washed five times with PBS. To optimize cell seeding efficiency, the PUR scaffolds were placed in 48-well plates, and a glass ring was held down to prevent the PUR scaffolds from floating up in the medium. Then, 50 μL of different doses of hAESC cells (1×10^6 cells/mL, 2×10^6 cells/mL, 4×10^6 cells/mL, 6×10^6 cells/mL) were added to the PUR scaffolds, respectively, after 24 h of incubation, live and dead cells were identified by double staining with Calcein-AM and PI (Calcein-AM/PI). To measure the PUR loading efficiency, hAESC cells with Cy5.5 fluorophores were loaded in the PUR in a 48-well plate. After 15 min, 2 h and 24 h, PUR with the hAESC cells (50 μL hAESCs at 4×10^6 cells/mL) were transferred to another well. The fluorescence intensity in the original wells was measured by imaging to evaluate cells leaked out from the PUR scaffold. A total of 50 μL of hAESCs at 4×10^6 cells/mL was added to each PUR scaffold, which were then transferred into a 48-well culture plate and maintained for 2 h in a 37 °C, 5% CO_2 incubator for initial adhesion. Then, 1 mL of complete culture medium was added slowly to each along the well wall to avoid shock the adherent cells on the scaffolds and incubated continuously.

To assess the morphology of hAESCs on the PUR porous scaffold, scaffold containing hAESC cells were cultured for 24 h and then washed three times with PBS. After fixed with 4% paraformaldehyde and penetrated with 0.5% Triton-X-100, Rhodamine-Phalloidin (Yeasen, Cat# 40734ES75) was used to stain the cytoskeleton of hAESCs growing on the surface of the PUR scaffold. Meantime, samples were dehydrated with an anhydrous ethanol/tertiary butanol gradient. Samples were lyophilized and examined by SEM. For the proliferation of hAESCs in PUR scaffold, the cell viability of hAESCs after cultured in patches at 1, 3, and 5 days was detected using the CCK-8 test (Beyotime, Cat# C0037).

For the migration assay of hAESCs in PUR scaffold, the depth of hAESCs in the porous scaffold at 1, 3, and 5 days was measured using confocal laser scanning microscopy (CLSM, ZEISS LSM880, Germany). At each time point, hAESCs were stained with calcein and washed with PBS for 3 times, then fixed with 4% paraformaldehyde at 37 °C for 1 h, followed by washing with PBS for three times. The observed hAESCs in confocal images were invading from the top of the porous scaffolds. The migration depth of cells was the distance between the appearance of fluorescence and the disappearance of fluorescence.

For the cell model of oxygen glucose deprivation (OGD) injury and TUNEL (TdT-mediated dUTP Nick-End Labeling, Roche, Cat# 11684817910) analysis, hAESCs cultured with or without PUR were subjected to hypoxia in vitro in an oxygen control cabinet (Thermo Fisher Scientific, 51030287), using a mixture of 95% nitrogen, 1% hydrogen, and 5% CO_2 to create hypoxia. hAESCs were treated with OGD by culturing in the culture medium without serum and glucose and under hypoxic condition (<1% O_2) for 5 h as previously reported[57]. Then, the apoptotic cell observation was detected using live/dead staining and TUNEL staining. For live/dead cell staining of hAESCs in the porous scaffold, hAESCs were seeded in the scaffold and incubated for 24 h. Each well was gently washed with PBS three times and then incubated with Calcein and EthD-1 for 40 min (Invitrogen, LIVE/DEAD Viability/Cytotoxicity Kit, Cat# L3224). Fluorescence images were observed using a fluorescence microscope (IX81, Olympus) and showed the distribution of dead and live cells in the porous scaffold. The live cells showed green, and dead cells showed red.

MI animal model and implantation of patches in vivo

All animal experiments were approved by the Laboratory Animal Welfare and Ethics Committee of Zhejiang University (Ethics Code: ZJU20210074). Male SD rats (180 ± 20 g, six weeks old) were purchased from Zhejiang Academy of Medical Sciences. The MI model was established according to a previous study[30]. Briefly, after being anesthetized with 1% sodium pentobarbital by intraperitoneal injection and placed in the supine position after endotracheal intubation, rats were provided with assisted ventilation on a sterile operating table by a small animal ventilator. The heart was exposed through a left thoracotomy and excised pericardium before ligating the left anterior descending (LAD) coronary artery with a 6–0 suture. After coronary artery ligation, a pale discoloration of the myocardium below the ligation site suggested that the MI model was successfully established. After successful ligation, the rats were randomly divided into six groups: Sham, MI, hAESC injection (2×10^5 cells), and TPU-hUMSC patch (polycarbonate-based thermoplastic polyurethanes, TPUs, CAT#PC-3572D, Lubrizol), PUR- hUMSC patch and PUR-hAESC patch groups. Cardiac patches seeded with hAESC or hUMSC cells (2×10^5 cells/patch) were implanted onto the infarcted region and secured by continuous running suture with 6–0 polypropylene. The chest wall, muscle and skin layer were carefully sutured by layer with 3–0 sutures.

Labelling of hAESCs

To trace the implanted hAESCs in vivo, hAESCs were pre-labeled with CellTracker CM-Dil (Invitrogen, Cat# C7000) with red fluorescence. Briefly, hAESCs were incubated at 37 °C for 5–8 min in DMEM/F12 media with 2 g/mL CM-Dil and then transferred to 4 °C for 15 min.

Bioluminescence imaging for hAESC tracking in vivo

hAESC cells were transfected with Fluc$^+$GFP$^+$ lentivirus (LVCON451, Shanghai Genechem co., Ltd) for 48 h before cocultivation with the PUR porous patch. The hAESCs and PUR-hAESC patch groups were selected to dynamically track the survival and retention of transplanted hAESCs in vivo. The rats were imaged at 1, 3, 5 and 7 d post-surgery by the in vivo imaging system (Caliper Life Sciences, USA)[58]. Briefly, D-fluorescein (15 mg/mL, 2 mL per rat, Beyotime, Cat# ST196) was injected into the recipient rat's intraperitoneal cavity. After 10 min, the rats were anesthetized with isoflurane in oxygen, and placed into the imaging chamber and imaged immediately. Image signals were quantified and regarded as representative of the total amount of cells present.

Quantitative real-time RT-PCR

Hearts from MI or PUR-hAESC operated rats at 7 and 28 days after surgery were collected for RNA extraction. The total RNAs were extracted from infarction region with an E.N.Z.A. Spin Column Animal Total RNA Purification Kit (Sangon Biotech, China, Cat# B518651) as described in the manufacturer's instructions. One microgram of RNA was subjected to cDNA synthesis with Evo M-MLV RT Master Mix (Accurate Biology, China, Cat# AG11706). Quantitative real-time PCR (SYBR Green Pro Taq HS qPCR kit, Accurate Biology, China, Cat# AG11701) was performed with the BioRad iCycler real-time PCR detection system (Bio-Rad, Hercules, CA, USA) with the primers provided in Supplementary Table 1 and was carried out in triplicate in at least three independent experiments. Fold differences in the expression level of each gene were calculated using CT values. To normalize expression levels, the housekeeping gene, glyceraldehyde 3-phosphate dehydrogenase (GAPDH) was used as an internal control.

Tissue collection and $CD45^+$ cells isolation

Left ventricles of hearts from the MI and PUR-hAESC groups were collected and minced into fine pieces (including the infarcted and peri-infarcted regions). Tissues were enzymatically digested with collagenase A and elastase at 37 °C rotationally. After dissociation, cell suspensions were passed through a 30 μm cell strainer, followed by red blood cell lysis (Solarbio, Cat# R1010). For sorting of all the immune cells ($CD45^+$), the digested suspensions were stained with Propidium Iodide (Beyotime, Cat# ST511) and FITC anti- rat CD45 antibody (BioLegend Cat# 202205, RRID: AB_314005) (isotype control was FITC Mouse IgG1, Cat# 400107, RRID: AB_326429), and sorted on a FACS Aria III (BD Biosciences, Franklin Lakes, NJ) with a 100 μm nozzle.

Single cell sequencing

$CD45^+$ cells were sorted using FACS from single-cell suspensions of hearts of MI- or PUR-hAESC-operated rats 7 days after surgery. After washing and resuspending in 0.5 mL cold PBS, purified $CD45^+$ cells were processed in the Chromium single cell gene expression platform (10× Genomics). Briefly, Single Cell 3′ Reagent Kit v2 was used to generate droplets encapsulating single cell and barcoded beads. Following capture and lysis, reverse transcription was performed in a thermal cycler (ProFlex PCR). cDNA was synthesized and amplified for 14 cycles. The amplified-cDNA was fragmented, ligated with adapter and sample index, and selected with SPRI beads (Beckman). Sequencing was performed on the NovaSeq 6000 Illumina sequencing platform. Bioinformatic analysis was performed using the OmicStudio tools at https://www.omicstudio.cn/tool.

Cardiac function assessment

Rats were examined by the VEVO2100 ultrasound system (Visual Sonics, Canada) at 7 d and 28 d post-surgery under isoflurane anesthetization to observe the left ventricular (LV) function. The echocardiography operator was blinded to the experimental design performed the procedure. After adequate two-dimensional images been obtained, the M-mode cine loops of a long-axis was positioned, left ventricular fractional shortening (LVFS), the left ventricular ejection fraction (LVEF), end-diastolic left ventricular volume (EDV) and end-systolic left ventricular volume (ESV) were calculated using computer algorithms.

Histology and immunohistochemistry

After conventional anesthesia, hearts were harvested and washed with PBS for three times to remove blood, and then placed in 10% KCl. Hearts were fixed overnight with 4% paraformaldehyde, then embedded in paraffin and sectioned. H&E staining (Solarbio, Cat# G1120) was performed according to the manufacturer's specification. Masson's trichrome staining (Solarbio, Cat# G1346) was performed to evaluate the fibrotic area by delineating the blue-stained collagen scar tissue and red-stained cardiac muscle with ImageJ (https://imagej.nih.gov/ij/).

For immunohistochemistry, Proteins of interest in the samples were targeted with the following primary antibodies after an overnight incubation at 4 °C: mouse anti-cTnT (Abcam Cat# ab8295, RRID:AB_306445), rabbit anti-Ki67 (Abcam Cat# ab15580, RRID:AB_443209), rabbit anti-CD31 (Abcam Cat# ab222783, RRID: AB_2905525), mouse anti-α-SMA (Abcam Cat# ab8211, RRID: AB_306359), rabbit anti-CD4 (Abcam, Cat# ab237722), mouse anti-CD8 (Abcam Cat# ab33786, RRID:AB_726709), rabbit anti-MPO (Abcam Cat# ab9535, RRID:AB_307322), rabbit anti-S100a9 (Abcam Cat# ab242945, RRID:AB_2876886), mouse anti-CD68 (Bio-Rad Cat# MCA341GA, RRID:AB_566872), rabbit anti-Hif-1α (Abcam Cat# ab114977, RRID:AB_10900336) rabbit anti-SPP1(Abcam Cat# ab63856, RRID:AB_1524127), rat anti-CD68 (Bio-Rad Cat# MCA1957GA, RRID:AB_322219), rabbit anti-Nrp1 (Abcam Cat# ab81321, RRID: AB_1640739), mouse anti-Nur77 (Santa Cruz Cat# sc-365113, RRID: AB_324217), rabbit anti-VEGFA (Abcam Cat# ab52917, RRID:AB_883427), rabbit anti-Col1 (Abcam Cat# ab270993, RRID:AB_2927551). The corresponding secondary antibodies: Alexa Fluor 594-conjugated donkey anti-rabbit IgG (Jackson ImmunoResearch, Cat# 711-586-152, RRID:AB_2340622), Alexa Fluor 594-conjugated donkey anti-mouse IgG (Jackson ImmunoResearch, Cat# 715-586-150, RRID:AB_2340857), Alexa Fluor 488-conjugated donkey anti-rabbit IgG (Jackson ImmunoResearch, Cat# 711-546-152, RRID:AB_2340619) and Alexa Fluor 488-conjugated donkey anti-mouse IgG (Jackson ImmunoResearch, Cat# 715-545-150, RRID:AB_2340846). DAPI (Sigma, USA) was used for nuclear staining. All images were obtained by the SLIDEVIEW VS200 digital slide scanner (VS200, Olympus).

Oxidative injury and cell apoptosis

Electron paramagnetic resonance (EPR) test and lipid peroxidation assay: One day post-surgery, infarcted tissue from the heart was collected and frozen in liquid nitrogen, and then ground. First, an EPR spectrometer (Bruker EMXplus X-band EPR spectrometer) was used to detect the ROS-related free radical signal of milled myocardial tissues at the 3372 G magnetic field. The signal peak between 3330 and 3380 G was double-integrated using Bruker BioSpin WinEPR Acquisition software to calculate the signal integral area per gram of tissues, which represents the ROS level in the infarct area. Malondialdehyde (MDA) assay: MDA is a product of lipid oxidative degradation. The infarcted myocardial tissues were homogenized in lysis solution at 4 °C, and the homogenate was centrifuged at 9000 g for 10 min at 4 °C. The total protein concentration in the supernatant was determined using a bicinchoninic acid (BCA) assay kit (Beyotime Biotechnology). MDA concentration (nmol/mg protein) in the supernatant was quantified by MDA assay kit (Beyotime Biotechnology).

Cell Apoptosis: The hearts of Sham, MI, TPU-hUMSC, PUR-hUMSC and PUR-hAESC groups one day post-surgery were harvested and rinsed three times in PBS and fixed in 4% (w/v) formaldehyde, then embedded in paraffin wax. The cell apoptosis was evaluated by terminal deoxynucleotidyl transferase dUTP nick end labeling (TUNEL) staining. The percentage of apoptotic cells was calculated by quantifying TUNEL positive cells and normal cells using the Image J software.

Production of hAESC-conditioned media

The following genes were selected from hAESCs to knockdown: oxidation resistance (SOD1, GSS, CAT, PRDX1), immune modulation (IL1R2, CD59, PTGES, MIF) angiogenesis (Angiogenin1, VEGFA, PDGFB) and ECM remodeling (MMP9, CTSB, BMP1). hAESCs (2×10^6) were seeded onto 10 cm dishes, following growth to 40–50% confluency, and were transfected with siRNA at a concentration of 50 nM. All siRNA sequences were presented in Supplementary Table 2. All transient transfections used Hieff Trans®siRNA (Yeasen, China), following the manufacturer's protocol. After 6 h, the culture media were replaced with DMEM/F12 containing 10% KSR,1% anti-anti,1% L-glutamine,1% NEAA and 1% sodium pyruvate. The conditioned-medium was collected after 24 h and centrifuged at 800 g for 10 min at 4 °C to remove cellular debris.

Cytoprotective effects of hAESC conditioned media

To investigate whether hAESCs conditioned media could provide cellular protection against ischemic injury, 50% hAESCs-conditioned media (NC-si, SOD1-si, GSS-si, CAT-si, PRDX1-si, S/G/C/P-si) was added into H9C2 (GNR 5, Cell Bank of Typical Culture Collection of Chinese Academy of Sciences) culture containing hydrogen peroxide (H_2O_2) (500 µM). Following 1 h exposure to H_2O_2, H9C2 were harvested and were examined by using Annexin V−FITC kit (cat# C1062M, Beyotime) to measure the apoptosis. In addition, Reactive Oxygen Species (ROS) assay (ROS Assay Kit, cat# S0033M Beyotime) was performed to measure ROS level. Briefly, DCFH-DA was diluted with serum-free culture medium at a ratio of 1:1000 and H9C2 cells were incubated in a 37 °C cell culture incubator for 20 min. Wash cells three times with serum-free cell culture medium, then detected using flow cytometry.

Immunomodulation effect of hAESC conditioned media

RAW264.7 cells (ATCC) were seeded in a 6-well plate with a density of 1×10^6/well overnight. Then 1 µg/mL Lipopolysaccharide (LPS) (Sigma) was used to induce macrophage polarization for 24 h with or without the co-culture of 50% hAESC-conditioned media (IL-NC-si, IL1R2-si, CD59-si, PTGES-si, MIF-si, I/C/P/M-si). Then, RAW264.7 cells and supernatants were collected for qPCR and ELISA analysis for pro-inflammatory factors, including IL-β, IL-6 and TNF-α, following the manufacturer's protocol (Lianke bio). All primers sequences were presented in Supplementary Table 1.

The effect of hAESC conditioned media on myocardial fibroblast activation

Neonatal rat myocardial fibroblasts were isolated from the right and left ventricles of one-week old male or female SD rats. Upon cutting the rat thoracic cavity to expose the heart, ice-cold phosphate buffered saline was injected into the RV through the aorta. The heart was removed and cut into small pieces (to not exceed 2 mm in diameter), then washed three times by DMEM at 500 g for 5 min. The tissue was plated into pre-coated 0.02% collagen I dish and cultured in DMEM with 10% FBS, 1% L-glutamine and 1% anti-anti in the incubator with 5.0 % CO_2 at 37 °C. After 3 days, cells crawled out from the edges of tissue and filled the dish. Cells from passages 3 and 4 were used in differentiation experiments. Neonatal rat myocardial fibroblasts were starved overnight in serum-free medium. Differentiation of myofibroblasts was stimulated by 10 ng/ml TGF-β1 (Abclonal, China), and then incubated with 50% hAESC-conditioned media (NC-si, BMP1-si, CTSB-si, MMP-9-si, B/C/M-si). Following culture 48hs, cells were collected for immunofluorescence (α-SMA, COL1), qPCR (α-SMA, COL1, CTGF and FN1) and western blotting (WB) analysis (α-SMA, COL1). All primers sequences were presented in Supplementary Table 1. For WB, the following primary antibodies were used: rabbit anti rat α-SMA (abclonal, Cat# a1011, 1:1000, RRID: AB_2757633), rabbit anti rat Col1 (abclonal, Cat# a1352, 1:1000, RRID: AB_2760381), mouse anti rat GADPH (abclonal, Cat# ac002, 1:1000, RRID: AB_2736879).

Human endothelial cell migration and tube formation

Endothelial cell migration assay: Human umbilical vein endothelial cells (HUVECs) were cultured in 6-well plates (10×10^4 cells/well) with EGM-2 medium (Lonza, Cat# CC-3156). When HUVECs had grown to an appropriate density, a straight line was scratched with the 1-mL pipette tip perpendicular to the bottom surface of the well. Subsequently, 50% hAESCs-conditioned media (NC-si, VEGFA-si, angiopoietin1-si, PDGFB-si, V/A/P-si) was added to the experimental group, and the migration area was digitally photographed at 0, 6, 12, and 24 h; the area of the cell-free gap was calculated using ImageJ (version 6.0, NIH). The migration rate was determined and expressed as a percentage of closure relative to the initial size at 0 h.

Tube-formation assay: The basement membrane matrix Matrigel (Corning, Cat# 354277) was added to a 24-well plate and solidified by incubation at 37 °C for 30 min. HUVECs (4×10^4) were plated onto each well containing Matrigel with EGM-2 medium and incubated at 37 °C for 6 h. The experimental group contained 50% hAESCs-conditioned media (NC-si, VEGFA-si, angiopoietin1-si, PDGFB-si, V/A/P-si), and tube structures were evaluated via microscopy.

Statistical analysis

Statistical analysis was performed using GraphPad Prism 9 (San Diego, USA). Results are shown as mean ± standard deviation. Unpaired *t* test, one-way ANOVA and two-way ANOVA were employed to compare the results among groups. *p* value of <0.05 was considered significant.

Reporting summary

Further information on research design is available in the Nature Portfolio Reporting Summary linked to this article.

Data availability

All data supporting the findings of this study are available within the paper, its Supplementary Information, and source data file. Single-cell sequence data that support the findings of this study are available through the National Center for Biotechnology Information Gene Expression Omnibus (NCBI GEO) under accession code GSE237527. The mass spectrometry proteomics data have been deposited to the ProteomeXchange Consortiumvia the iProX partner repository with the dataset identifier PXD043861. Further information and requests for resources and reagents should be directed to and will be fulfilled by the lead contact Luyang Yu (luyangyu@zju.edu.cn) on request. Source data are provided with this paper.

References

1. Moran, A. E. et al. The global burden of ischemic heart disease in 1990 and 2010: the Global Burden of Disease 2010 study. *Circulation* **129**, 1493–1501 (2014).
2. Reed, G. W., Rossi, J. E. & Cannon, C. P. Acute myocardial infarction. *Lancet* **389**, 197–210 (2017).
3. Forte, E., Furtado, M. B. & Rosenthal, N. The interstitium in cardiac repair: role of the immune-stromal cell interplay. *Nat. Rev. Cardiol.* **15**, 601–616 (2018).
4. Yang, Y. et al. Activin receptor-like kinase 4 haplodeficiency alleviates the cardiac inflammation and pacing-induced ventricular arrhythmias after myocardial infarction. *Aging* **13**, 17473–17488 (2021).
5. Ong, S. B. et al. Inflammation following acute myocardial infarction: Multiple players, dynamic roles, and novel therapeutic opportunities. *Pharm. Ther.* **186**, 73–87 (2018).
6. Saxena, A., Russo, I. & Frangogiannis, N. G. Inflammation as a therapeutic target in myocardial infarction: learning from past failures to meet future challenges. *Transl. Res.* **167**, 152–166 (2016).
7. Huang, S. & Frangogiannis, N. G. Anti-inflammatory therapies in myocardial infarction: failures, hopes and challenges. *Br. J. Pharm.* **175**, 1377–1400 (2018).
8. Zhu, D. et al. Minimally invasive delivery of therapeutic agents by hydrogel injection into the pericardial cavity for cardiac repair. *Nat. Commun.* **12**, 1412 (2021).
9. Jiang, B., Yan, L., Shamul, J. G., Hakun, M. & He, X. Stem Cell Therapy of Myocardial Infarction: A Promising Opportunity in Bioengineering. *Adv. Therapeutics* **3**, 1900182 (2020).

10. Segers, V. F. & Lee, R. T. Stem-cell therapy for cardiac disease. *Nature* **451**, 937–942 (2008).
11. Almeida, S. O., Skelton, R. J., Adigopula, S. & Ardehali, R. Arrhythmia in stem cell transplantation. *Card. Electrophysiol. Clin.* **7**, 357–370 (2015).
12. Alam, P. et al. Cardiac Remodeling and Repair: Recent Approaches, Advancements, and Future Perspective. *Int. J. Mol. Sci.* **22**, 13104 (2021).
13. Lee, C. Y. et al. Therapeutic Potential of Stem Cells Strategy for Cardiovascular Diseases. *Stem Cells Int.* **2016**, 4285938 (2016).
14. Vagnozzi, R. J. et al. An acute immune response underlies the benefit of cardiac stem cell therapy. *Nature* **577**, 405–409 (2020).
15. Peng, H., Shindo, K., Donahue, R. R. & Abdel-Latif, A. Cardiac Cell Therapy: Insights into the Mechanisms of Tissue Repair. *Int. J. Mol. Sci.* **22**, 1201 (2021).
16. Magatti, M., Vertua, E., Cargnoni, A., Silini, A. & Parolini, O. The Immunomodulatory Properties of Amniotic Cells. *Cell Transplant.* **27**, 31–44 (2018).
17. Liu, Q.-W. et al. Characteristics and Therapeutic Potential of Human Amnion-Derived Stem Cells. *Int. J. Mol. Sci.* **22**, 970 (2021).
18. Li, J. et al. Subretinal Transplantation of Human Amniotic Epithelial Cells in the Treatment of Autoimmune Uveitis in Rats. *Cell Transpl.* **27**, 1504–1514 (2018).
19. Tan, B. et al. Therapeutic effect of human amniotic epithelial cells in murine models of Hashimoto's thyroiditis and Systemic lupus erythematosus. *Cytotherapy* **20**, 1247–1258 (2018).
20. Huang, Q. et al. Placental chorionic plate-derived mesenchymal stem cells ameliorate severe acute pancreatitis by regulating macrophage polarization via secreting TSG-6. *Stem Cell Res. Ther.* **12**, 337 (2021).
21. Miki, T. Stem cell characteristics and the therapeutic potential of amniotic epithelial cells. *Am. J. Reprod. Immunol.* **80**, e13003 (2018).
22. Toda, A., Okabe, M., Yoshida, T. & Nikaido, T. The Potential of Amniotic Membrane/Amnion-Derived Cells for Regeneration of Various Tissues. *J. Pharmacol. Sci.* **105**, 215–228 (2007).
23. Liu, Y. et al. The Protective Benefit of Heme Oxygenase-1 Gene-Modified Human Placenta-Derived Mesenchymal Stem Cells in a N-Nitro-L-Arginine Methyl Ester-Induced Preeclampsia-Like Rat Model: Possible Implications for Placental Angiogenesis. *Stem Cells Dev.* **30**, 991–1002 (2021).
24. Akle, C. A., Welsh, K. I., Adinolfi, M. & Leibowitz, S. Immunogenicity of Human Amniotic Epithelial-Cells after Transplantation into Volunteers. *Lancet* **2**, 1003–1005 (1981).
25. Yeager, A. M. et al. A therapeutic trial of amniotic epithelial cell implantation in patients with lysosomal storage diseases. *Am. J. Med. Genet* **22**, 347–355 (1985).
26. Zhang, Q. & Lai, D. Application of human amniotic epithelial cells in regenerative medicine: a systematic review. *Stem Cell Res. Ther.* **11**, 439 (2020).
27. Magatti, M., Vertua, E., Cargnoni, A., Silini, A. & Parolini, O. The Immunomodulatory Properties of Amniotic Cells:The Two Sides of the Coin. *Cell Transplant.* **27**, 31–44 (2018).
28. Yang, P. J. et al. Biological characterization of human amniotic epithelial cells in a serum-free system and their safety evaluation. *Acta Pharm. Sin.* **39**, 1305–1316 (2018).
29. Rudman, J. & Frishman, W. H. Stem Cell Therapy for Acute Myocardial Infarctions: A Systematic Review. *Cardiol. Rev.* **28**, 140–147 (2020).
30. Yao, Y. et al. ROS-responsive polyurethane fibrous patches loaded with methylprednisolone (MP) for restoring structures and functions of infarcted myocardium in vivo. *Biomaterials* **232**, 119726 (2020).
31. Yao, Y. et al. Multifunctional elastomer cardiac patches for preventing left ventricle remodeling after myocardial infarction in vivo. *Biomaterials* **282**, 121382 (2022).
32. Wang, W. et al. Rebuilding Postinfarcted Cardiac Functions by Injecting TIIA@PDA Nanoparticle-Cross-linked ROS-Sensitive Hydrogels. *ACS Appl. Mater. Interfaces* **11**, 2880–2890 (2019).
33. Zhang, D. et al. Biocompatible Reactive Oxygen Species (ROS)-Responsive Nanoparticles as Superior Drug Delivery Vehicles. *Adv. Healthc. Mater.* **4**, 69–76 (2015).
34. Boateng, S. Y. et al. RGD and YIGSR synthetic peptides facilitate cellular adhesion identical to that of laminin and fibronectin but alter the physiology of neonatal cardiac myocytes. *Am. J. Physiol. Cell Physiol.* **288**, C30–C38 (2005).
35. Ban, K. et al. Cell Therapy with Embryonic Stem Cell-Derived Cardiomyocytes Encapsulated in Injectable Nanomatrix Gel Enhances Cell Engraftment and Promotes Cardiac Repair. *ACS Nano* **8**, 10815–10825 (2014).
36. Yuan, Z. et al. Injectable Citrate-Based Hydrogel as an Angiogenic Biomaterial Improves Cardiac Repair after Myocardial Infarction. *ACS Appl. Mater. Interfaces* **11**, 38429–38439 (2019).
37. Dick, S. A. et al. Self-reing resident cardiac macrophages limit adverse remodeling following myocardial infarction. *Nat. Immunol.* **20**, 29–39 (2019).
38. Raimondi, C., Brash, J. T., Fantin, A. & Ruhrberg, C. NRP1 function and targeting in neurovascular development and eye disease. *Prog. Retin Eye Res.* **52**, 64–83 (2016).
39. Wang, Y. et al. Cardiomyopathy and Worsened Ischemic Heart Failure in SM22-α Cre-Mediated Neuropilin-1 Null Mice. *Arteriosclerosis Thrombosis Vasc. Biol.* **35**, 1401–1412 (2015).
40. Hilgendorf, I. et al. Ly-6C Monocytes Depend on Nr4a1 to Balance Both Inflammatory and Reparative Phases in the Infarcted Myocardium. *Circ. Res.* **114**, 1611–1622 (2014).
41. Ha, C. H. et al. Protein kinase D-dependent phosphorylation and nuclear export of histone deacetylase 5 mediates vascular endothelial growth factor-induced gene expression and angiogenesis. *J. Biol. Chem.* **283**, 14590–14599 (2008).
42. Ong, S., Rose, N. R. & Cihákova, D. Natural killer cells in inflammatory heart disease. *Clin. Immunol.* **175**, 26–33 (2017).
43. Sun, K., Li, Y. Y. & Jin, J. A double-edged sword of immunomicroenvironment in cardiac homeostasis and injury repair. *Signal Transduct. Tar.* **6**, 79 (2021).
44. Frangogiannis, N. G. The inflammatory response in myocardial injury, repair, and remodelling. *Nat. Rev. Cardiol.* **11**, 255–265 (2014).
45. Hussen, K. A. et al. CD4CD8T-Lymphocytes in Xenogeneic and Human Graft-versus-Host Disease. *Front. Immunol.* **11**, 579776 (2020).
46. Overgaard, N. H., Jung, J. W., Steptoe, R. J. & Wells, J. W. CD4/CD8 double-positive T cells: more than just a developmental stage? *J. Leukoc. Biol.* **97**, 31–38 (2015).
47. Egawa, T. Fateful Decision in the Thymus Controlled by the Transcription Factor ThPOK. *J. Immunol.* **206**, 1981–1982 (2021).
48. Hess, N. J. et al. Inflammatory CD4/CD8 double-positive human T cells arise from reactive CD8 T cells and are sufficient to mediate GVHD pathology. *Sci. Adv.* **9**, eadf0567 (2023).
49. Zheng, B. et al. Trajectory and Functional Analysis of PD-1 CD4CD8 T Cells in Hepatocellular Carcinoma by Single-Cell Cytometry and Transcriptome Sequencing. *Adv. Sci.* **7**, 2000224 (2020).
50. Bohner, P. et al. Double Positive CD4 CD8 T Cells Are Enriched in Urological Cancers and Favor T Helper-2 Polarization. *Front. Immunol.* **10**, 622 (2019).
51. Marrero, Y. T. et al. Immunophenotypic characterization of double positive T lymphocytes in Cuban older adults. *Exp. Gerontol.* **152**, 111450 (2021).
52. Tang, J. N. et al. Cardiac cell-integrated microneedle patch for treating myocardial infarction. *Sci. Adv.* **4**, eaat9365 (2018).
53. Fox, I. J. et al. Use of differentiated pluripotent stem cells in replacement therapy for treating disease. *Science* **345**, 889-+ (2014).

54. Kehl, D. et al. Proteomic analysis of human mesenchymal stromal cell secretomes: a systematic comparison of the angiogenic potential. *Npj Regen. Med.* **4**, 8 (2019).
55. Montgomery, M. et al. Flexible shape-memory scaffold for minimally invasive delivery of functional tissues. *Nat. Mater.* **16**, 1038-+ (2017).
56. Xie, J. et al. Alleviating Oxidative Injury of Myocardial Infarction by a Fibrous Polyurethane Patch with Condensed ROS-Scavenging Backbone Units. *Adv. Healthc. Mater.* **11**, e2101855 (2022).
57. Xing, M. et al. Strontium ions protect hearts against myocardial ischemia/reperfusion injury. *Sci. Adv.* **7**, eabe0726 (2021).
58. Chen, J. et al. Chitosan/silk fibroin modified nanofibrous patches with mesenchymal stem cells prevent heart remodeling post-myocardial infarction in rats. *Acta Biomater.* **80**, 154–168 (2018).

Acknowledgements

This work was supported by the Zhejiang Provincial Key R&D Program of China (2022C03097-L.Y., 2022C01106-C.G.), the National Natural Science Foundation of China (82370450-L.Y., 82300296-J.L., 81770444-L.Y., 81600354-Cong.Q, 81970372-Cong.Q, 11932017-Cong.Q, 82202328-Y.Z.), the China Manned Space Flight Technology Project Chinese Space Station (YYWT-0901-EXP-06-L.Y.), National Key R&D Program of China (2018YFA0800504-L.Y., 2019YFE0117400-Y.Z.), the Zhejiang Provincial Basic Public Welfare Research Program of China (LTGD24H020002-Z.G.), the Medical and Health Science and Technology Program of Zhejiang Provincial Health Commission of China (2021KY633-Z.G., 2022KY725-Z.G.), the Fundamental Research Funds for the Central Universities of China (K20220228-L.Y.). and the State Key Laboratory of Transvascular Implantation Devices, China (012024018-Y.Z.). We thank Dr. She-long Zhang and Dr. Fang-liang Huang (Equipment and Technology Service Platform, College of Life Sciences, Zhejiang University) for their excellent technical support with microscopy and flow cytometry.

Author contributions

Conceptualization: L.Y., C.G., Y.Z., J.L. and Y.Y.; methodology and investigation: J.L., Y.Y., J.Z., L.S., Y.K. and P.L.; animal studies: J.L., Y.Y., Jia. L., Y.L., J.X. and T.J.; data acquisition: J.L., Y.Y., J.Z., Z.Y. and C.Q.; writing—original draft preparation, J.L., Y.Y. and C.Q.; writing—review and editing, L.Y., C.G., Y.Z. Z.G. and Cong.Q.; funding acquisition, L.Y., C.G., Y.Z., Z.G., Cong.Q. and J.L. All authors have read and agree to the published version of the manuscript.

Competing interests

The authors declare no competing interests.

Additional information

Supplementary information The online version contains supplementary material available at https://doi.org/10.1038/s41467-024-53531-8.

Correspondence and requests for materials should be addressed to Yang Zhu, Changyou Gao or Luyang Yu.

Peer review information *Nature Communications* thanks Narutoshi Hibino, and the other, anonymous, reviewer(s) for their contribution to the peer review of this work. A peer review file is available.